Which feature influences on-eye power change of soft toric contact lenses: design or corneal shape?

Tamsin Doll[1], Joshua Moore[1,2], Ahmad H Shihab[1,3], Bernardo T Lopes[1,4], Ashkan Eliasy[1], Osama Maklad[1], Richard Wu[5,6], Lynn White[7], Steve Jones[1], Ahmed Elsheikh[1,8,9], Ahmed Abass[1]*

[1] School of Engineering, University of Liverpool, Liverpool, UK

[2] Department of Mathematical Sciences, University of Liverpool, Liverpool, UK

[3] School of Engineering, University of Hertfordshire, Hatfield, UK

[4] Department of Ophthalmology, Federal University of Sao Paulo, Sao Paulo, Brazil

[5] Department of Optometry, Central Taiwan University of Science and Technology, Taichung, Taiwan

[6] College of Optometry, Pacific University, Oregon, USA

[7] Ultravision CLPL, Leighton Buzzard, UK

[8] School of Biological Science and Biomedical Engineering, Beihang University, Beijing, China

[9] National Institute for Health Research (NIHR) Biomedical Research Centre at Moorfields Eye Hospital NHS Foundation Trust and UCL Institute of Ophthalmology, London, UK

* Corresponding Author: Dr Ahmed Abass, School of Engineering, University of Liverpool, Liverpool, L69 3GH, UK. A.Abass@liverpool.ac.uk

Abstract

Purpose: This study investigates how both the peripheral zone design and corneal shape affect the behaviour of soft contact lenses on-eye.

Methods: In this study, soft contact lenses of varying nominal cylindrical powers and peripheral zone designs — a single-prism gravity-based stabilised lens (G1P), two-prism blink-based stabilised lens (B2P) and four-prism blink-based stabilised lens (B4P) — were generated as finite element models. The on-eye simulation results were analysed to identify the impact of each peripheral zone design (Each with different volume ratios) on the effective power change (EPC) when worn by a subject. Topographies of three eyes of varying average simulated anterior corneal curvature (flat, average & steep) were used in this study.

Results: The volume of the lens's peripheral zone as a ratio of the total lens volume (V_p) recorded very weak correlations with the effective power change (EPC) among the three investigated designs when they were fitted to the flat eye (R=-0.19, -0.15 & -0.22 respectively), moderate correlations with the average eye (R=0.42, 0.43 & 0.43 respectively) and strong correlations with the steep eye (R=0.91, 0.9 & 0.9 respectively). No significant differences were noticed among the three investigated designs and none of the cylindrical lenses designed with axis 90° recorded EPC values outside the acceptance criteria range (ACR) of ±0.25 D. No significant differences in EPC were recorded among the three designs G1P, B2P and B4P (p>0.6) when they were designed with three axes at 90°, 45° and 0°. Moving the toric lens axis away from 90° dragged the EPC to the negative side and most of the investigated lenses with axes at 45° and 0° recorded EPCs outside the ±0.25D range.

Conclusions: In all cases, the shape of the cornea had a more dominant effect on EPC when compared to the peripheral zone design. Corneal shape influences the soft toric contact lens's on-eye power change more than the lens design.

Introduction

Contact lenses are medical devices worn by over 150 million people worldwide [1]. Soft-structured contact lenses consist of two main zones; the optic zone designed to achieve the required refractive power that have few parameters for adjustment, and the peripheral zone which is designed to keep the lens on the eye using several geometric parameters [2]. In soft contact lens design, the peripheral zone is a specific region connecting the optic zone to the edge profile. This zone is substantial in contact lens fitting; it has been shown that the peripheral corneal shape has a more significant role in successful contact lens wear than the central radius of curvature of the cornea [3, 4]. Also when a soft contact lens is fitted to a cornea, it is the peripheral zone that flexes and deforms most [5] which may then influence the optic zone, to which it is connected. Any deformation of the optic zone will, in turn, affect the optical power profile. This change in lens power is termed effective power change (EPC). Mostly, soft lenses fitting approaches lack scientific basis compared to Rigid Gas Permeable (GP) lenses [6]. In the published literature, designers did not go into the scientific details of why certain soft lenses design patterns work better than others. The actual physical characteristics of the lens were either overlooked when calculating refractive optical power [7, 8] or simplified to theoretical statements of flexure hypotheses or empirical models [9-16].

In spherical soft contact lens designs, the peripheral zone is normally rotationally symmetrical and has a uniform thickness in all polar directions, thus changes are expected to be transmitted almost symmetrically. However, in toric lenses, the design requirement to avoid rotation [17] has led to the design of various stabilisation methods [18] which result in non-symmetrical areas of thickness in the peripheral zone. As the regional increased thickness influences the mechanical behaviour of the peripheral zone. It follows that the central optic zone also flexes in different ways depending on the stabilisation design, which affects the optical power profile. The question arises as to whether this change would affect the lens's refractive power significantly.

To determine the EPC in soft contact lenses when worn on-eye, a few techniques have evolved in the literature [5]. Strachan et al [6] proposed a technique to demonstrate the effect of lens geometry on the power of the lens on-eye. To achieve this, they used the ratio between the lens base curve and the radius of the cornea. For a more comprehensive review of the optical properties used in contact lens design, the reader is referred to Whittle et al [19].

Current market trends show an overall move towards disposable lenses [20]. Although some monthly lenses have a relatively wide parameter range, daily disposable lenses are constrained by the method of manufacture (injection moulding), and often offer no more than two base curves and one diameter — in fact, most brands only offer one base curve. As the flexure of the peripheral zone, will depend on the overall curvature of the cornea, it might be expected that some wearers will experience poor fitting [21] or an EPC, as outlined previously. Additionally, this change may be more pronounced for toric soft contact lenses due to the thickness changes and the influence of the stabilisation design.

The three most common soft toric stabilisation designs in the market are: (1) single prism (commonly known as prism ballast) or gravity-based stabilisation (G1P), Fig 1a; (2) two-prism blink-based stabilisation (B2P), Fig 1b; and (3) four-prism blink-based stabilisation (B4P), Fig 1c.

In addition to the main requirement of correcting refractive errors, soft contact lenses are designed to fit the eye. Although the design of the optic zone is restricted by the refractive power prescription, the design of the periphery zone has been left to the soft contact lens designer to construct using experience and common sense. There has been comparatively little work performed on peripheral zone design when compared to the research which has been conducted on the optic zone [22, 23].

The contact lens's capacity to refract light (refractive power) is a function of its surface shape and its refractive index which is constant for any material. As a soft contact lens settles on the eye, it changes its surface curvature as a result of being subject to the eyelid pressure and the tear surface tension force. For this reason, the soft contact lens's refractive power on-eye is not the same as it is off-eye,

104   where the lens is designed, manufactured and passed its quality control final inspection. The design

105   of the peripheral zone affects the flexure of the whole soft contact lens and hence, affects the EPC

106   within the optic zone. Thus, the results of this study explain unexpected requirements for over-

107   refraction for certain subjects seen in clinical practice, depending on their corneal shape.

108

109   The first peripheral zone design investigated in this study was the G1P, which is widely used in the

110   contact lens industry and comprises a thicker section at the bottom of the contact lens. This design

111   works with gravity to stabilise the lens automatically since the lower half is thicker, and therefore

112   heavier, than the rest of the lens. The G1P design assumes that the weight of the thicker portion

113   reacts with gravity such that when the centre of gravity is directly beneath the centre of rotation, the

114   moment is reduced to zero, and so the lens stabilises in this position [24]. This type of stabilisation

115   has minimal eyelid interaction and has the disadvantage of causing lens mis-location if the head is

116   moved from the vertical.

117   B2P designs evolved from the early forms of "dynamic stabilisation" where the upper and lower

118   portions of the lens were thinned to create a horizontal band of thicker material which interacted with

119   the eyelids [25]. This design evolved into specific zones at 3 and 9 o'clock positions which interact

120   with the lids in a more controlled fashion.

121   B4P designs [26] replace each prism zone with two smaller ones placed above and below the

122   horizontal plane in order to interact with the eyelids more directly [27] and have advantages over other

123   toric designs under a range of viewing conditions [28]. To gain a tangible perspective of how the three

124   lenses change when placed on eyes, they needed to be tested on a range of different shaped corneas.

125   The optimal soft contact lens adaptation, which allows patients' comfort, good quality of vision and

126   minimal interference with ocular surface functions and metabolism, is the result of a delicate balance

127   between eye and lens dimensions and mechanical properties.

128   In order to simulate different contact lens fitting scenarios, three sets of eyes and contact lens fits

129   were modelled by considering flat, average and steep corneas, the selection of eyes was carried out

130   considering Gilani's population study [29], where the median of the flat power simulated keratometry

131 (Sim-K) was 43.8 D, and the bounds of "flat" and "steep" corneas were determined by applying one

132 standard deviation of ±1.38 D. Both axial and tangential curvature maps of the three eyes used in this

133 study are presented in Fig 2. Additionally, the trigonometries behind these maps are given in Appendix

134 (A).

135 This study investigates the effect of employing three different peripheral zone stabilisation designs on

136 the EPC then determines which feature influences on-eye EPC, the eye shape or the contact lens

137 design. Although the authors' previous studies have been conducted on the effect of contact lens

138 power on EPC [5, 30], this work introduces a new and more relevant approach, where the eye is not

139 considered as a rigid solid body. In terms of design, the lenses considered in this study are designed

140 using three peripheral zone designs, whereas the previous studies [5, 30] only considered a single

141 peripheral zone. Previous studies [5, 30] employed lenses that, despite being valid designs, do not

142 match those that are used in the soft contact lenses industry. The current work utilises lenses with a

143 reduced concave geometry, thus allowing for improved tear circulation and for better compatibility

144 with those used in the industry.

Materials and methods

Participants

147 The presented record review used fully anonymised secondary data, which according to the University

148 of Liverpool's Policy on Research Ethics, ethical approval was unnecessary. Nevertheless, the study

149 followed the tenets of the Helsinki Declaration of 1964 (revised in 2013). Written informed consent

150 was also provided in the primary data collection by all participants for the use of their de-identified

151 data in scientific research [31].

152 In order to represent the normal corneal shape range, three sets of corneal topographies obtained

153 using an Eye Surface Profiler (ESP) (Eaglet Eye BV, Houten, The Netherlands) from three subjects

154 were selected for processing in this study. These were classified as flat, average and steep corneas

155 [32] in terms of their flat simulated keratometry readings (flat-K): the average eye was within 0.5 SD

156 of the average flat-K, the flat and the steep eyes were below or above 1.5 SD [29]. The "flat" and

157   "steep" corneal shapes were taken from the right eyes of 28 and 25-year old females respectively

158   (Flat Sim-K = 41.8 D & 46.8 D, Astigmatism = -0.17 D & -1.9 D, Angle = 2° & 3°). The "average"

159   corneal shape was taken from the left eye of a 24-year old male (Flat Sim-K = 43.8 D, Astigmatism =

160   -1.7 D, Angle = 3°). The selection of suitable eyes for inclusion in the study was carried out based on

161   the corneal topography population study of Gilani [29]. Accordingly, the median of the "average" Sim-

162   K was set to 43.8 D, and the bounds of flat and steep corneas were determined by applying one

163   standard deviation of ±1.38 D [29]. By applying this classification to the patient data set, the corneas

164   were classified as "flat" if the flat meridian power was less than or equal to 42.4 D, "steep" for flat

165   meridian power of 45.2 D or above, and "average" if it was in-between. Recorded data was reviewed

166   and three eyes from healthy participants were selected for this study, based on their geometry.

167

Data processing

169   The eyes' surface data was exported from the ESP software in the form of MATLAB (MathWorks,

170   Natick, USA) binary data container format (*.mat) where the characteristics of eyes, as measured by

171   the ESP system were extracted. Each selected eye's topography data was processed by custom-built

172   MATLAB codes completely independent from the built-in ESP software digital signal processing

173   algorithms. Each eye's topography data was measured over more than 250,000 points on average.

174   The ESP data comprises the anterior front-surface of the eye up to 20 mm without extrapolation. The

175   Z-axis represents the axial direction of the eye with an origin point resting on the corneal apex with

176   the eye on the negative side. In order to determine the cornea's asphericities, conic models were

177   fitted to each cornea's anterior surface of the flat, average and steep eyes where asphericity q and

178   corresponding shape factor $k = q + 1$ were obtained. The asphericity factor q is synonymous to the

179   overall curvature of the cornea, with positive values leading to increased steepness and negative

180   values inducing a flattening effect [33, 34]. Fitting was carried out by minimising the mean squares

181   error between the corneal surface and the fitted conic model for each eye. The corneal models

182   considered in this study utilised radii of 7.45, 7.04 & 6.42 mm, asphericities of q =-1.2, -1.107 & -

183   1.154 and corresponding shape factors k= -0.2, -0.107 & -0.154 for the flat, average and steep eyes

184   respectively.

185   The scleral portion of the measured eye's topography data was separated from the corneal portion

186   by detecting the limbus position. The detected limbal position on the eye's anterior surface was then

187   identified through the three-dimensional (3D) non-parametric method introduced by Abass et al. in

188   2018 [35]. The limbus detection algorithm was based on the fact that the cornea and the sclera have

189   different curvatures [36] and the limbus is the boundary where the corneal curvature changes to match

190   that of the scleral globular shape [37]. Therefore, the position of the limbus was detected by locating

191   the turning point of the raw elevation 2nd derivative at each meridian.

192

193   When the limbus was detected; the scleral topography data was first processed through an edge-

194   effect elimination process where topographical artefacts caused by the eyelash's interference or tear

195   pooling were removed using the technique introduced by Abass et al. [31]. Once the scleral

196   topographical data is cleared of measurement artefacts, it was then fitted to a sphere using the least

197   squares error method, minimising the fitting error Err for every point i of the n points as described in

198   Eq. 1

$$Err = \sum_{i=1}^{n}\left((X_i - X_c)^2 + (Y_i - Y_c)^2 + (Z_i - Z_c)^2 - R_s{}^2\right)^2 \qquad \text{Eq. 1}$$

199   Where X_i, Y_i and Z_i are the scleral height data, X_c, Y_c and Z_c are the best-fitted sphere's centre

200   coordinates, and R_s is the radius of the sclera.

201   To construct a 3D eye geometrical model without losing the precision of the measured part of the

202   sclera, the measured portion of the anterior sclera was used in the construction process while the

203   best-fitted spherical surface was only used in the areas where no scleral surface measurements were

204   available. The constructed eye geometry was then used to build the finite element model as will be

205   shown later in this study.

206

Contact lens design

The back and front-surfaces of soft contact lenses modelled in this study were configured to approximate those that are commercially available. However, simulation of the specific design of particular brands was not possible, as this is protected non-available information. Despite this, the precise engineering principles of soft contact lens design were carefully considered in this study.

Each lens surface was divided into an optical zone and a peripheral zone (Fig 3). The front-surface was designed to achieve three main requirements; the necessary optical power within the optic zone of the lens, stabilisation through a balance prism profile (T_w) and a specified edge thickness (T_e) at the point where the peripheral zone merges into the edge profile.

Finally, due to clinical considerations, practical reasons and manufacturing restrictions, lenses cannot be designed with sharp edges when two zones meet. To mitigate this, any sharp edges must be smoothed. This study presents the mathematical details of how the geometry and locations of these fillets were determined.

A custom-built MATLAB script was written to generate the geometrical shape of the lenses based on the type of balance zone design, the design parameters and the optical power values. Although the design process has been covered in previous studies [5, 30], for completeness, details of the lens design are presented in Appendix (B). In addition to the details dealt with in previous work, the fillet design and new peripheral zone design techniques are also outlined (see S1).

Finite element modelling

In this study, soft contact lens models were fitted on three eye models representing flat, average and steep profiles, for a total number of 567 FE models with an average central processing unit (CPU) time of 12.2 min per model while a 4-core processor HP tower workstation (HP Inc UK Limited, Reading, UK) was being used. FE overall simulation wall-clock time was estimated as 117.3 hrs with an average of 12.4 min per model. Sets of lenses' geometrical profiles were digitally generated

232 through the MATLAB software for the three investigated designs G1P, B2P and B4P before being

233 further processed to build an FE model for each lens. The cylindrical lens set was designed with 21

234 nominal powers ranging from -10 DC to 10 DC at cylinder axes 90°, 45°, and 0° in one dioptre optical

235 power step.

236

237 As the ESP can only measure the anterior surface of the eye and is not capable of measuring the

238 posterior cornea, the central corneal thickness (CCT) was taken as its reported average value of 0.55

239 mm [38] then increased to 0.70 mm and 0.56 mm at the peripheral corneal zone and equatorial ring

240 respectively [39, 40]. Additionally, at the posterior pole, the thickness was taken as 0.84 mm [41].

241 Ocular globe wall thickness was varied linearly with the elevation angle among the previously

242 mentioned regions. Eight-node first-order continuum solid hybrid brick elements 'C3D8H' were used

243 in one layer of elements to build the eye model and 2 layers to build the contact lens models in

244 ABAQUS (Dassault Systèmes, Vélizy-Villacoublay, France) FE software package licenced to the

245 University of Liverpool, UK. Normally, the in-vivo human eye globe topography is measured whilst the

246 eye is stressed due to the intraocular pressure (IOP) hence, cannot be used for modelling without

247 pre-processing. To achieve the eyes' stress-free geometry (at IOP=0 mmHg), eye globe models were

248 initially built with the inflated dimensions, then a stress-free adaptation of each model was calculated

249 individually by following the iterative method presented in [42]. In each case, the stress-free model

250 was computed by considering an average IOP of 15 mmHg [43] and a maximal node position error

251 less than 10^{-4} mm. Once the stress-free models were determined, they were pressurised to IOP=15

252 mmHg through a uniformly distributed static pressure on the internal surfaces of the eye globe model

253 to mimic the aqueous and vitreous behaviour. The ABAQUS nonlinear geometry option "NLGEOM"

254 was set to "ON" during the inflation process and subsequent steps. This option allows loads to be

255 applied incrementally, whilst updating the stiffness matrix for each increment. Hence ABAQUS allows

256 nonlinear materials to be used for certain parts without altering linear FE formulation for linear

257 materials of other parts of the model.

258   The FE mesh convergence study of eye's model was carried out through applying internal pressure

259   of 15 mmHg on the internal surface of 14 eye models, half of them are double-layered, then monitoring

260   the relevant anterior eye's apex displacement. Single layers models were constructed using 804,

261   5004, 20004, 80004, 180004, 320004 and 500004 nodes then inflated. Relevant apex displacement

262   in single-layer models were reduced by 0.0%, 3.0%, 3.8%, 4.7%, 4.7%, 4.7% and 4.7% respectively

263   while the 804-node model was taken as the datum. Double layers models were constructed using

264   1206, 7506, 30006, 120006, 270006, 480006 and 750006 nodes where apex displacement was found

265   to be reduced by 0.0%, 3.2%, 3.9%, 4.7%, 4.8%, 4.9% and -5.0% respectively while the 1206-node

266   model was taken as the datum. The outcomes showed that a number of the elements equal to 40000,

267   arranged in 200 rings (80004 nodes), in a single layer converged to the displacement of 201.545 μm

268   at the apex node and was selected as an optimal number of elements for this simulation as it

269   compromised between the computational resources and the accuracy of the solution.

270   The contact lenses mesh was tested by 10 Plano lenses models, five of them were single-layered

271   with 20166, 20526, 21846, 23966 and 26886 nodes and the other five models were double-layered

272   with 20247, 20787, 22767, 25947 and 30327 nodes respectively. All contact lenses models were

273   tested when being fitted to the selected 80004 node eye model while the lenses apex displacement

274   was recorded. Lenses apex displacement was reduced by 0.0%, 0.8 %, 1.0%, 1.1% and 1.2% in

275   single-layered models and by 0.0%, 0.8%, 1.0%, 1.0% and 1.0% in double-layered models

276   respectively.

277   The outcome demonstrated that models with the number of the elements equal to 11680 arranged in

278   20 rings (22767 nodes) in double layers converged to the displacement of 203.425 μm at the apex

279   node and was selected as the optimal number of elements for the lens in this simulation. Lenses were

280   designed with an optic zone diameter d_1=8 mm, balance zone diameter d_2=11.25 mm, overall

281   diameter d_3 = 14.5 mm, and base curve R_{1b}=8.2 mm.

282

283 The contact lens material was simulated with the properties of non-ionic hydrogel with 77% water

284 content (Contamac, Saffron Walden, England, UK) and the eyelid effect by a nonlinear dynamic upper

285 eyelid blink pressure of $P_1 = 8.0$ mmHg [44] applied dynamically to the front surface of the lens. This

286 application occurred 0.6 s after applying the IOP pressure in a normalised amplitude following Kwon's

287 high-speed camera characterisation of the blinking kinematics [45], Fig 4. The effect of the tear layer

288 was simulated by applying the surface tension of tear fluid of $P_2 = 43.6$ mPa [27] to the back surface

289 of the contact lens. Using the FE software ABAQUS, the full FE model consisted of two parts, the

290 contact lens and the eye with a single interface between them. Material models are detailed in

291 Appendix (C).

292 In the context of ABAQUS FE models, the anterior corneal surface and contact lens back-surface

293 were taken as master and slave surfaces respectively. The interaction between these surfaces was

294 further defined using a coefficient of friction of 0.01 [46]**.**

295 The displacement of the eye's equatorial nodes was constrained in the Z-direction, and both the

296 corneal apex and posterior pole nodes were constrained in the X-direction and Y-direction. The lens,

297 however, was constrained by preventing X and Y displacement at the optical centre, Table 1 & Fig 5.

298 Table 1: Finite element simulation parameters

Step	Description	Integration scheme	Loading condition	Time
1	Stress-free iterations [42]	Implicit	Static	Normalised increments (0:1)
2	Inflation, IOP = 15 mmHg [43]	Implicit	Static	Normalised increments (0:1)
3	Eyelid pressure 8.0 mmHg [44]	Implicit	Dynamic	0.6 s, see Fig 4 [45]
4	Surface tension 43.6 mPa [27]	Implicit	Static	Normalised increments (0:1)

299

300 Once the design phase was complete, and the dimensions of lenses were obtained, the volume of

301 the lenses' peripheral zones, which contains the stabilisation prisms, were calculated as a ratio (V_p)

12

302   of the total lens volume via the MATLAB "boundary" function. This value indicates how much material

303   was put in the peripheral zone compared to the overall material content of the contact lens.

304   **Light raytracing**

305   To measure the EPC incurred by the conformance of each soft contact lens to the cornea, the light

306   raytracing technique outlined in [30] was employed. A custom-built MATLAB script performing light

307   raytracing across the lens optic zone was written and validated using the AutoCAD software ®

308   (Autodesk, Inc., San Rafael, California, USA). This technique allows for the simulation of a large

309   number of light-rays as they travel through the lens, Fig 6b. Prior to the ray-tracing analysis, the

310   coordinates of the FE models, pre and post conformance, were exported and fitted to surfaces using

311   piecewise cubic interpolation. The direction of each light-ray before, during and after entering the lens,

312   was then deduced through the use of Snell's law [47].

313   The focal point was then identified by finding the average location at which the light-rays intersect the

314   optical axis, Fig 6a. The distance between this point and the lens apex was then calculated to yield

315   the focal length, f. When inverted, the focal length can be used to produce a value for the lens's

316   optical power. The difference in optical power produced by the lens after and prior to conformance

317   was taken as the effective power change, EPC. The validated light raytracing script was run for each

318   of the considered contact lens geometries, before and after fitting to the three corneal geometries.

319   This allowed for the identification of the EPCs and their standard deviations across the lens's optic

320   zone.

321   Acceptance criteria range (ACR) for the level of EPC that would initiate a clinically significant response

322   was set at ±0.25 DC for practical reasons, as this reflects the minimum change in power used in

323   clinical optometric refractions.

324   # Statistical analysis

325   The statistical analysis carried out on the results of this study was performed using the Statistics and

326   Machine Learning Toolbox of the MATLAB software. The null hypothesis, at 95.0% confidence level

327   testing, was used to investigate the inferences of the findings based on statistical evidence. The

328 normal distribution of the samples was confirmed using the Kolmogorov-Smirnov test via MATLAB

329 [48] then the two-sample t-test was applied to investigate whether there was a significance between

330 pairs of data sets and to confirm whether the assessed findings represent an independent record.

331 The probability value (p) is an element in the closed period 0.0 to 1.0 where values of p higher than

332 0.05 indicate the validity of the null hypothesis [49]. The MATLAB function 'ttest2' was used and the

333 returned p-value in addition to binary test decision for the null hypothesis. The correlation coefficient

334 used in this study (R) is a measure of the linear dependence of two variables [50]. R values below 0.3

335 were considered as an indication of weak correlations; R values in the range 0.3 to 0.7 were

336 considered as an indication of moderate correlations; and finally, R values above 0.7 were considered

337 as an indication of strong correlations [51].

338 ## Results

339 When evaluating the flat eye models, the correlation between effective power change, EPC, and

340 peripheral zone volume, V_p, was weak, Fig 7. This was evident in all three of the investigated

341 peripheral zone designs (G1P, B2P and B4P) where the correlation coefficients were -0.19, -0.15 and

342 -0.22 respectively. The correlations were, however, moderate in the average eye models (R=0.42,

343 0.43 and 0.43 respectively) and strong in the steep eye models (R=0.91, 0.9 and 0.9 respectively).

344

345 When the effect of the toric axis on the EPC was investigated for the three eyes, a proportional

346 relationship was found, Fig 8. Moreover, the correlation between V_p and EPC decreased slightly from

347 0.28 with an axis at 90° to 0.24 with the axis at 45° and the axis at 0°. Changing the toric lens axis

348 away from 90° induced a negative EPC. Additionally, investigated lenses with axes of 45° and 0°

349 generally recorded EPCs outside the ACR.

350

351 When the effect of the lens's central thickness T_c was explored, it was clear that, for positive nominal

352 powers (up to 10 DC), the effect of T_c on the EPC was counter to the effect of Vp and the inverse

353 correlations were found, R=-0.21, -0.46 and -0.62 for axis 90°, 45°, and 0° respectively. T_c recorded

354 no correlation with the EPC within the negative nominal power ranges (down to -10 DC). Both axes

355 45° and 0° cylindrical lenses recorded EPC below the ACR in most of the nominal cylindrical power

356 range, Fig 9. No significant differences were recorded among the three designs G1P, B2P and B4P

357 designed with axes of 90°, 45° and 0°.

358

Discussion

359

360

361 The study investigated the impact of different prism designs in terms of the EPC against the nominal

362 power of the contact lenses. Although the results showed that all of the investigated designs were

363 changing their power as a result of altering their shape on the eye, all three recorded EPC within the

364 ±0.25 DC range when fitted to the three eyes (flat, average, steep). When the influence of the

365 peripheral zone was investigated, it was clear that the V_p was more strongly correlated to the steep

366 (R≅0.9) and the average eyes (R≅0.43) than the flat eye (R≅0.26) regardless of the choice of

367 peripheral zone design. However, when the three eyes were fitted with cylindrical lenses with a

368 different axis, the correlation between the V_p and the EPC slightly decreased from 0.28 to 0.24 as the

369 axis was reduced from 90° to 0°.

370

371 Unlike in previous studies [5, 30] where the eye was treated as an elastic rigid body, the hyper-elastic

372 material properties and dynamics of the eye were considered through updating the modelling process.

373 This has been achieved by modelling the eye's material in four regions (cornea, anterior sclera,

374 intermediate sclera, and posterior sclera) with hyper-elastic Ogden models. This update also allowed

375 consideration of the whole eye geometry precisely instead of the anterior portion only, considering

376 the existence of the intraocular pressure (IOP) and applying the eyelid pressure dynamically as a

377 function of time [45] instead of considering it as a static load [5, 30].

378

379 In all investigated cases, the eye shape had more influence on the EPC than the peripheral zone

380 design. However, and not as previously reported [52], the volume of the peripheral zone was highly

15

381   correlated with the EPC in the moderate and steep eye population. Additionally, the central thickness

382   was only correlated with EPC in lenses with positive nominal power.

383   It was not clear that anterior eye shape influences on-eye EPC however, as the contact lens's design

384   has a limited effect of the on-eye refractive performance. Moreover, using the lens's central thickness

385   as an estimator for calculating EPC [52] is not possible with negative powered lenses, therefore, the

386   lens's peripheral zone ratio of the total lens volume could be used as a linear estimator for EPC.

387   However, the relationship between the V_p and the EPC is dependent on the eye shape.

388

389   In this study, the simulation of the soft contact lens performance on the eye was limited to observing

390   the deformation of the lens and the associated EPC on each corneal shape in response to applied

391   eyelid pressure. Increasing the number of eyes could strengthen statistical conclusions, however, the

392   three eyes used in this study were carefully selected from a database containing 125 pairs of eyes to

393   represent good examples of flat, average, and steep eyes and allow the study to vary contact lenses'

394   design with a practical number of models (567 models). In this study, the effect of the tear layer was

395   simplified and simulated by applying the surface tension of the tear fluid of 43.6 mPa [27] to the back

396   surface of the contact lens as no fluid-structure interaction analysis has been carried out in this study.

397   The rotation and translation of the soft contact lenses were not considered in the models used in this

398   study to simplify the convergence towards stable solutions in the ABAQUS FE software. It was not

399   possible to simulate accurate rotational effects of the contact lens as the current model does not

400   calculate extraneous factors such as tear volume, eyelid position and movement characteristics or

401   gravitational effects. Despite this, this study has highlighted the dependence of EPC on the corneal

402   geometry and demonstrated that, although specific designs can be used to reduce EPC, the corneal

403   geometry will have an overarching effect.

404

Declaration of interest

406   All authors of this article declare that they have no conflict of interest.

List of figures

Fig 1: Three designs of a soft contact lens with a base curve 8.2 mm, diameter 14.5 mm, spherical power -2.0 DS, cylindrical power +1.0 DC at axis 90° and central thickness 0.15 mm: (a) Gravity-based single-prisms stabilised lenses (G1P), (b) Blink-based two-prisms stabilised lenses (B2P), (c) Blink-based four-prisms stabilised lenses (B4P).

Fig 2: Axial and tangential curvature (Ra, Rt) maps of the flat, average, and steep eyes used in the current study.

Fig 3: Geometry parameters of a blink-based two-prisms stabilised lens (B2P) with base curve 8.2 mm, spherical power -2.0 DS, optical cylindrical power -1.0 DC, axis 90° and central thickness 0.2 mm. In this figure, fillets radii r_1 and r_2 were set to 2.5 mm and = 2.0 mm respectively. See Appendix (B) for more details.

Fig 4: Normalised eyelid pressure magnitude with time. This distribution is based on the palpebral aperture measurement as reported in [34].

Fig 5: Contact lens finite element model for a G1P lens design fitted to an average eye (IOP=15 mmHg) on the ABAQUS finite element software: (a) before fitting, (b) after fitting. Colour scale is representing the magnitude of the displacement (U) in mm. Eye's equatorial nodes were constrained in axial directions.

Fig 6: Light raytracing according to Snell's law in (a) a single meridian, (b) three-dimensional analysis (lens's thickness has been increased in this figure for displaying purposes).

Fig 7: Effective power change (EPC) for cylindrical lenses with axis 90° as a function of the peripheral zone volume (V_p) when fitted to the flat eye (1st column), average eye (2nd column), and steep eye (3rd column). The three investigated designs are plotted in rows.

Fig 8: Effective power change for lenses with axis 90°, 45°, and 0° as a function of the peripheral zone volume.

Fig 9: Effective power change for lenses with axis 90°, 45°, and 0° as a function of the lens's central thickness.

Fig 10: Determination of corneal surface axial radius of curvature (r) at a certain meridian plane. In this method, the centre of the curvature (c) is always restricted to the corneal visual axis.

Fig 11: Determination of corneal surface tangential radius of curvature (r) at a certain meridian plane. In this method, the centre of the curvature (c) is not restricted to the corneal visual axis.

Fig 12: A typical FE model for the average eye used in this study where different colours represent different material models. The eye's equatorial nodes were constrained in axial directions.

Fig 13: Stress-strain curves for the material models. Contact lens's material was modelled as a linear elastic material, however, the eye was modelled as a hyper-elastic material.
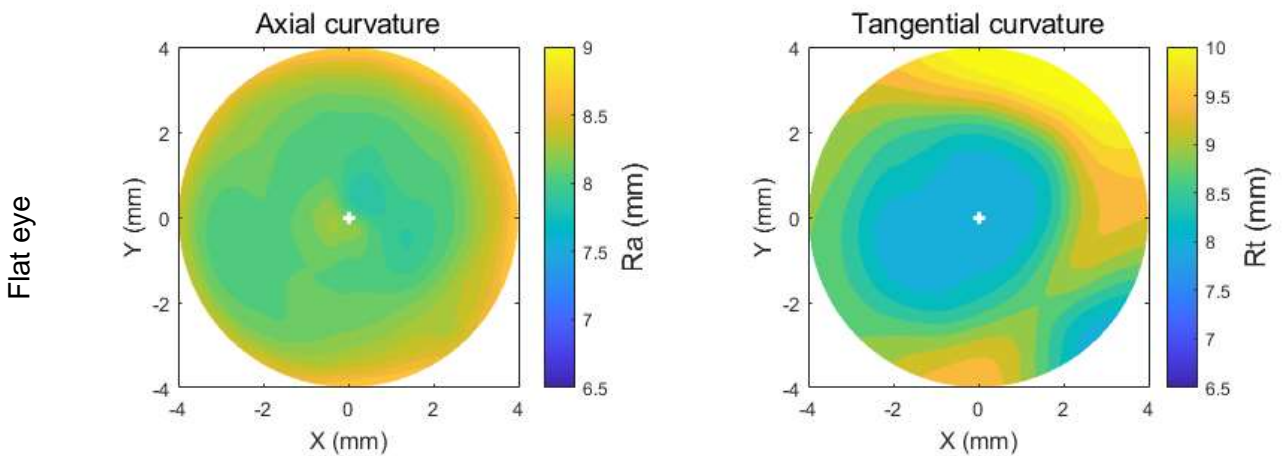
442

443

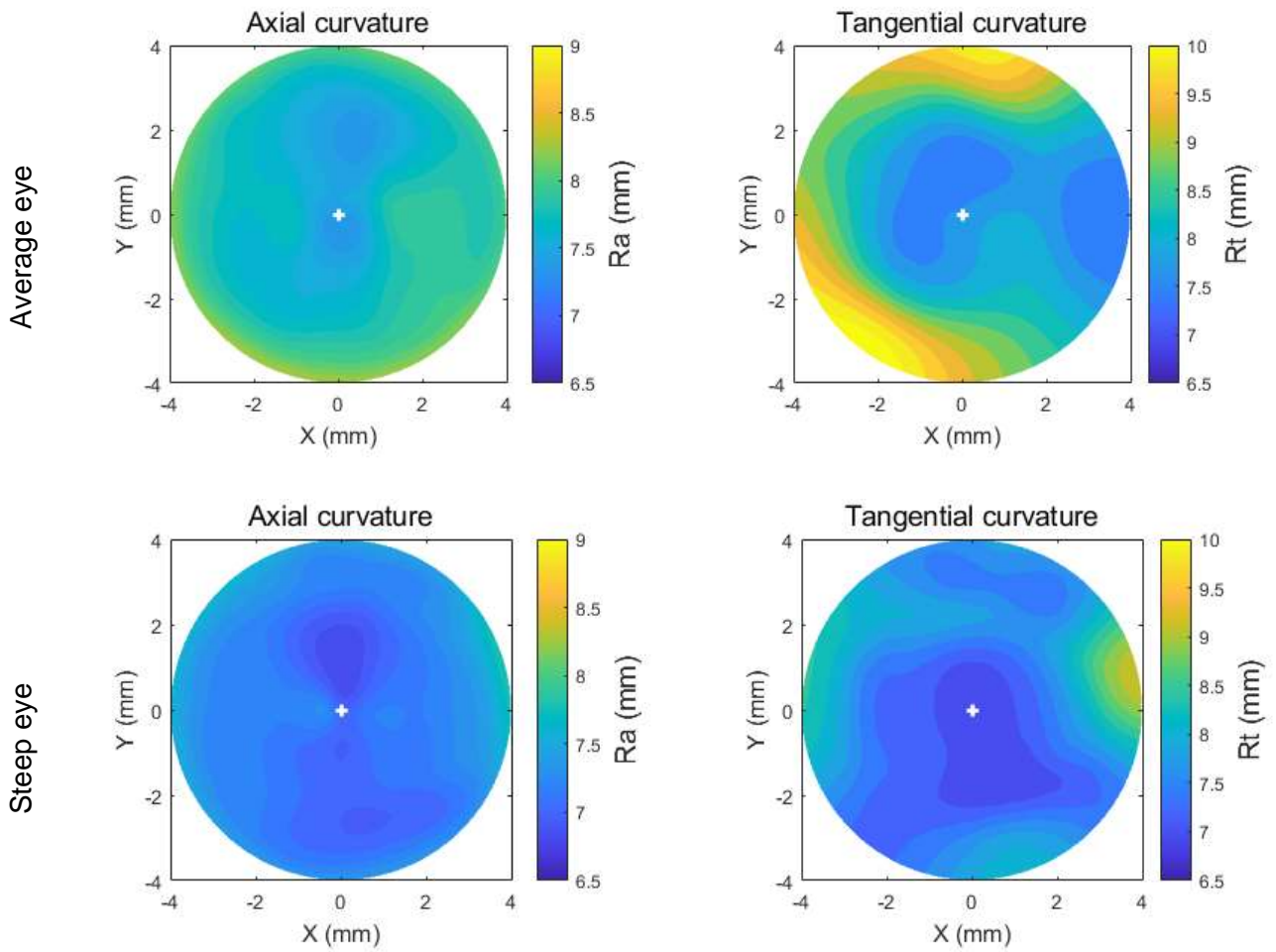(a)   (b)   (c)
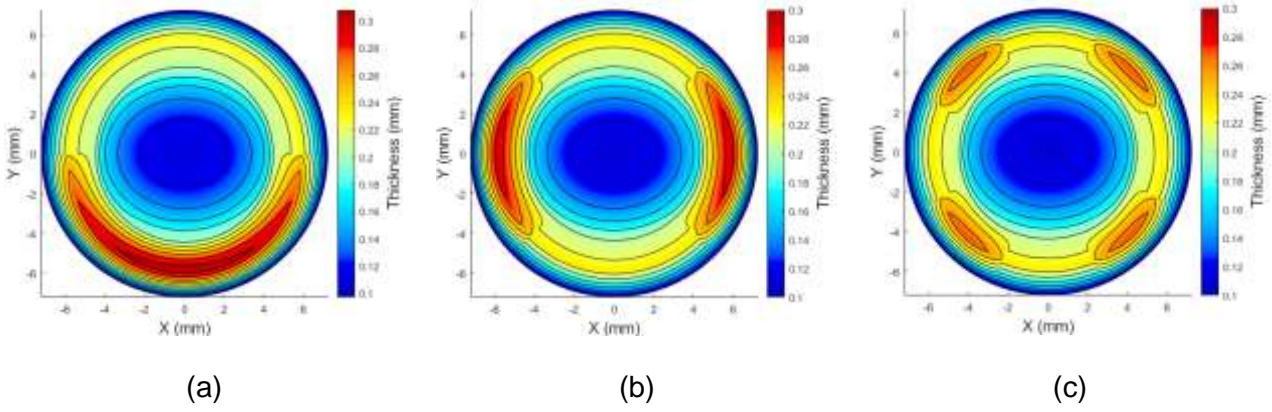
444 Fig 1: Three designs of a soft contact lens with a base curve 8.2 mm, diameter 14.5 mm, spherical

445 power -2.0 DS, cylindrical power +1.0 DC at axis 90° and central thickness 0.15 mm: (a) Gravity-

446 based single-prisms stabilised lenses (G1P), (b) Blink-based two-prisms stabilised lenses (B2P), (c)

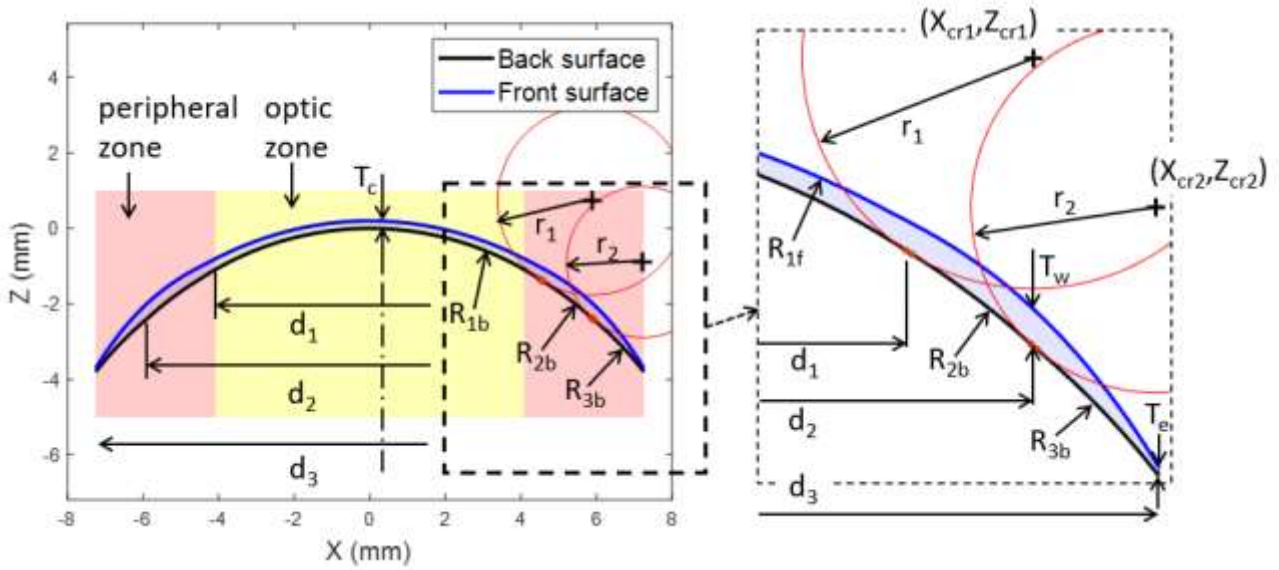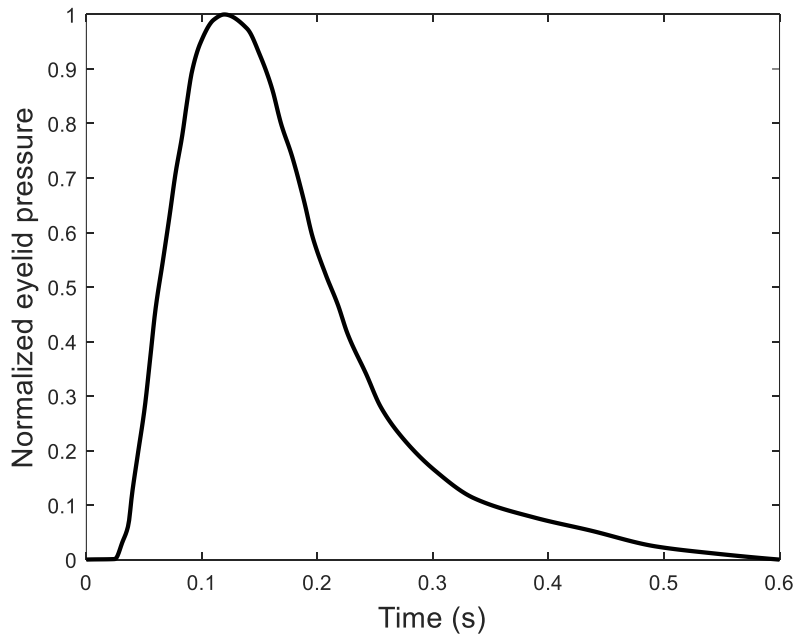447 Blink-based four-prisms stabilised lenses (B4P).

448

449

Fig 2: Axial and tangential curvature (Ra, Rt) maps of the flat, average, and steep eyes used in the current study.

455

Fig 3: Geometry parameters of a blink-based two-prisms stabilised lens (B2P) with base curve 8.2 mm, spherical power -2.0 DS, optical cylindrical power -1.0 DC, axis 90° and central thickness 0.2 mm. In this figure, fillets radii r_1 and r_2 were set to 2.5 mm and = 2.0 mm respectively. See Appendix (B) for more details.
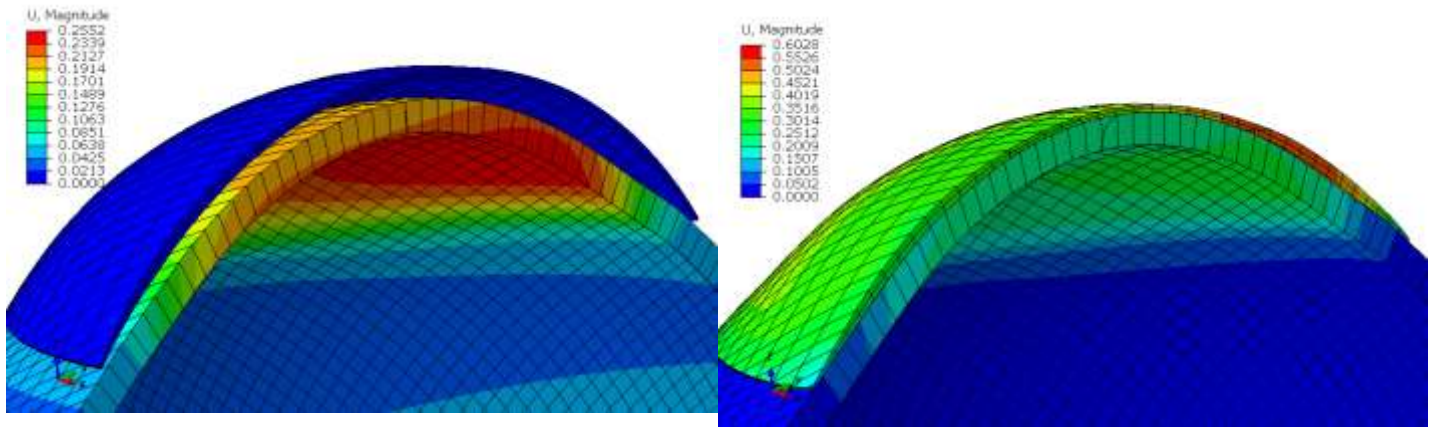
460

461

Fig 4: Normalised eyelid pressure magnitude with time. This distribution is based on the palpebral aperture measurement as reported in [45].
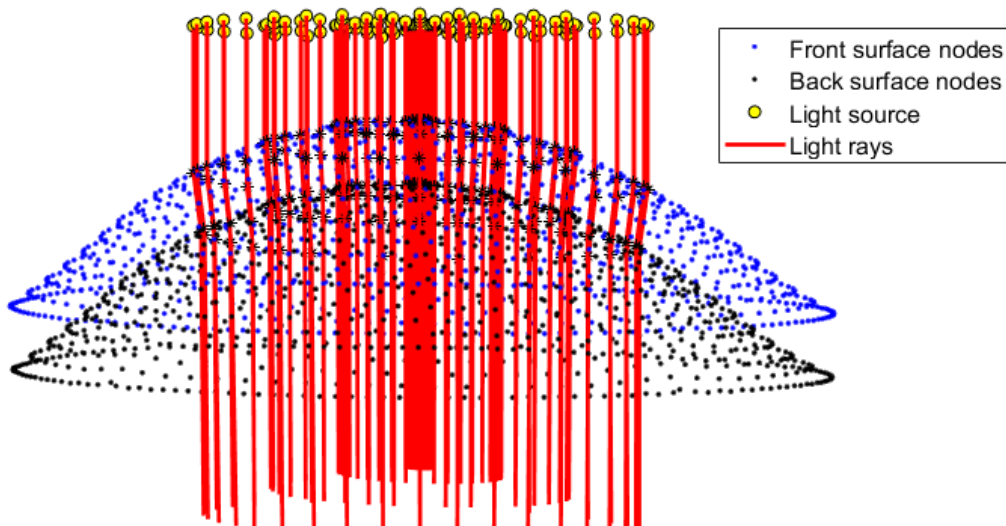
464

(a)   (b)

Fig 5: Contact lens finite element model for a G1P lens design fitted to an average eye (IOP=15 mmHg) on the ABAQUS finite element software: (a) before fitting, (b) after fitting. Colour scale is representing the magnitude of the displacement (U) in mm. Eye's equatorial nodes were constrained in axial directions.
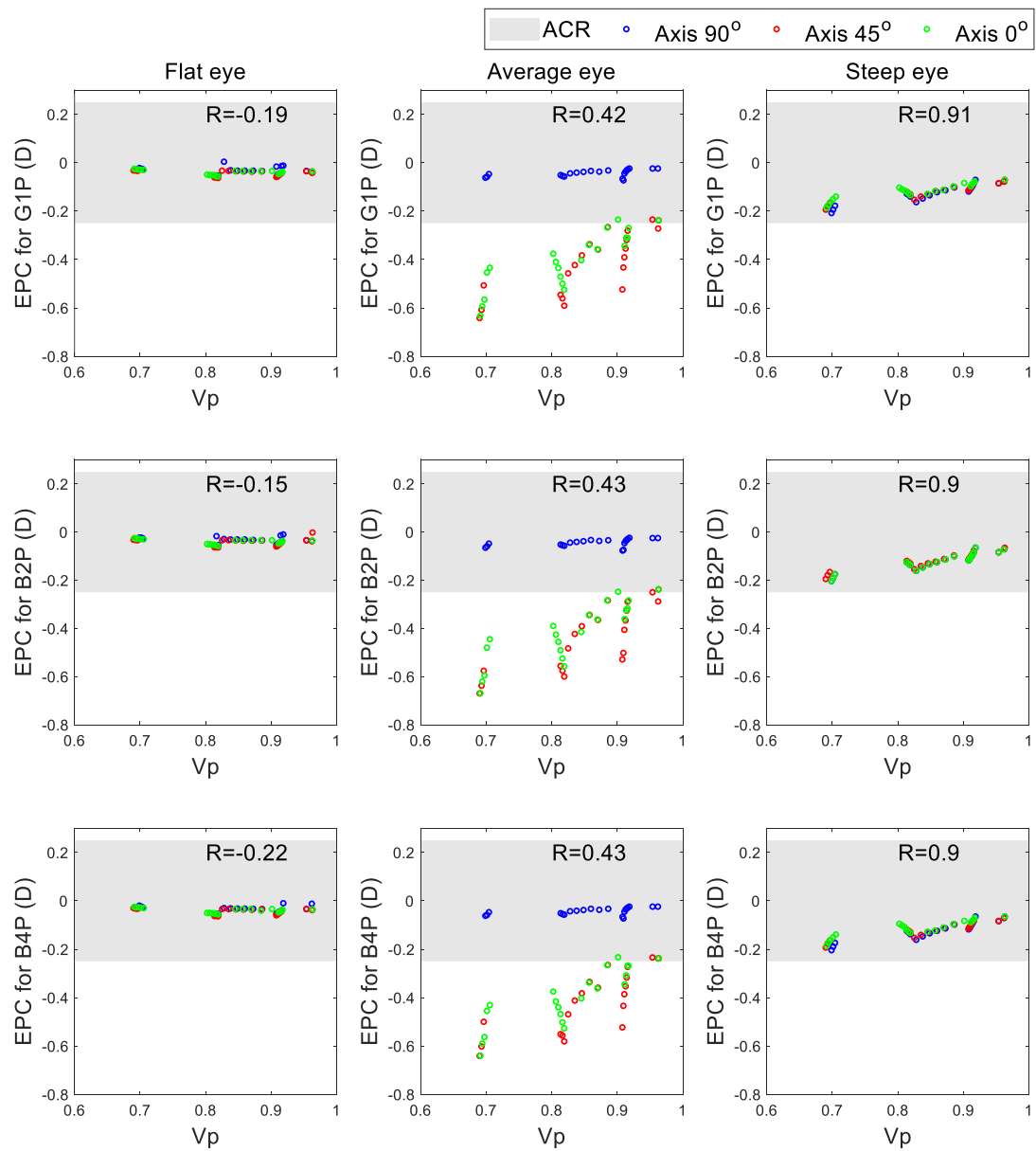
465

466
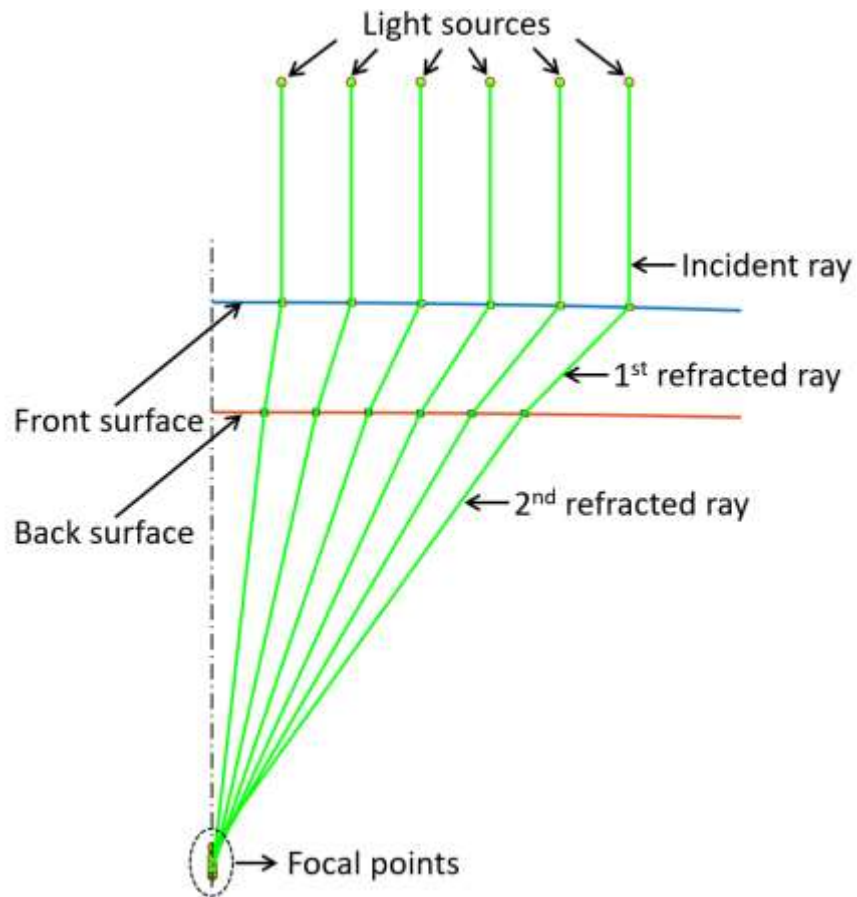
(a)

(b)

Fig 6: Light raytracing according to Snell's law in (a) a single meridian, (b) three-dimensional

analysis (lens's thickness has been increased in this figure for displaying purposes).

467

468

469　Fig 7: Effective power change (EPC) for cylindrical lenses with axis 90° as a function of the peripheral

470　zone volume (V_p) when fitted to the flat eye (1st column), average eye (2nd column), and steep eye (3rd

471　column). The three investigated designs are plotted in rows.

472

473

474
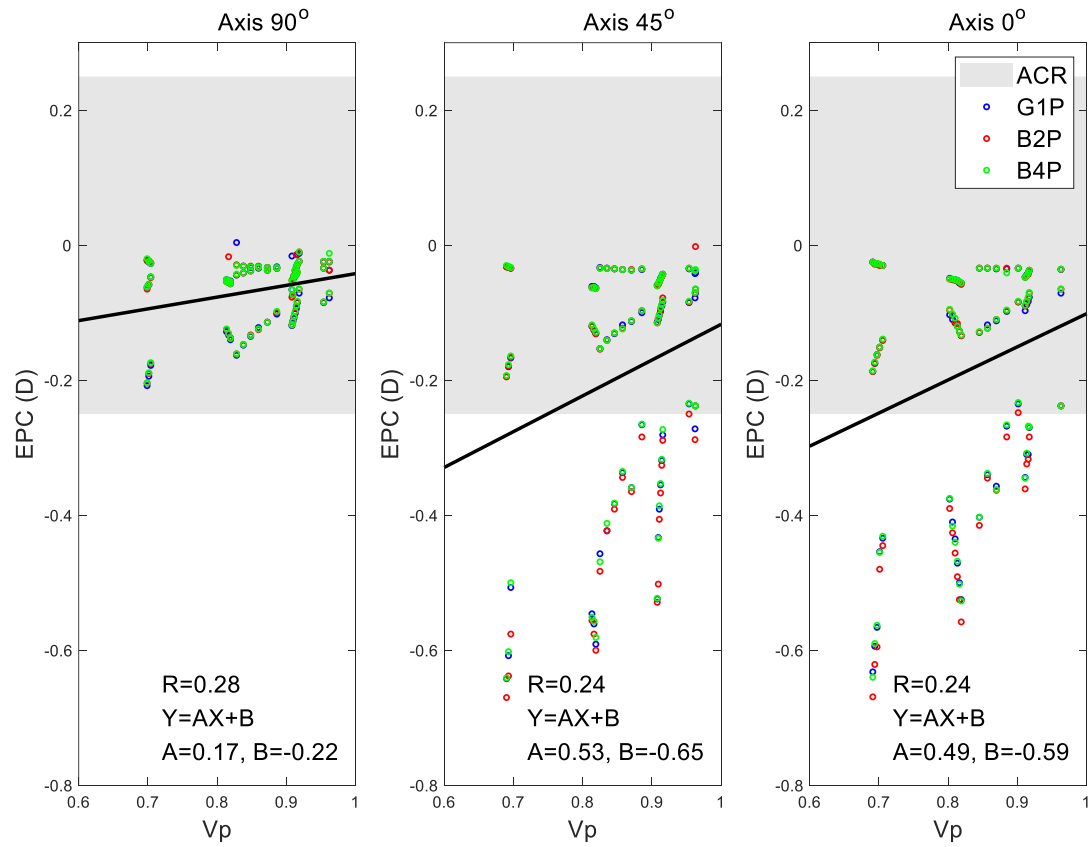
475

476 Fig 8: Effective power change for lenses with axis 90°, 45°, and 0° as a function of the peripheral zone
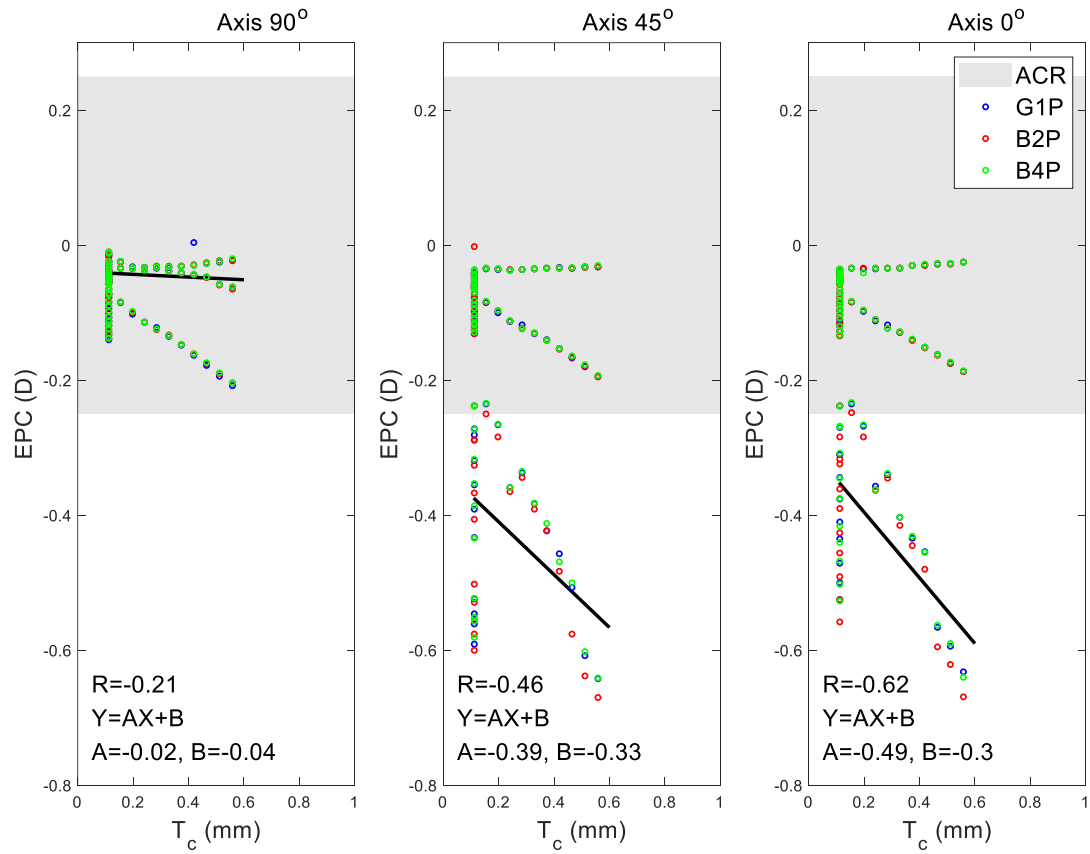
477 volume.

478

479

480

481

482

483

484

485

486

487

488

Fig 9: Effective power change for lenses with axis 90°, 45°, and 0° as a function of the lens's central

thickness.

References

1.	Moreddu R, Vigolo D, Yetisen AK. Contact Lens Technology: From Fundamentals to Applications. Advanced Healthcare Materials. 2019;8(15):1900368. doi: 10.1002/adhm.201900368.

2.	Phillips AJ, Speedwell L. Contact Lenses E-Book: Elsevier Health Sciences; 2018.

3.	Young G, Schnider C, Hunt C, Efron S. Corneal topography and soft contact lens fit. Optom Vis Sci. 2010;87(5):358-66. Epub 2010/04/14. doi: 10.1097/OPX.0b013e3181d9519b. PubMed PMID: 20386354.

4.	Sulley A, Lorenz KO, Wolffsohn JS, Young G. Theoretical fitting characteristics of typical soft contact lens designs. Contact Lens & Anterior Eye. 2017;40:248-52.

5.	Abass A, Stuart S, Lopes BT, Zhou D, Geraghty B, Wu R, et al. Simulated optical performance of soft contact lenses on the eye. PLOS ONE. 2019;14(5):e0216484. doi: 10.1371/journal.pone.0216484.

6.	Davis RL, Becherer PD. Techniques for Improved Soft Lens Fitting. Contact Lens Spectrum. 2005;August, 2005.

7.	Leube A, Kovats I, Wahl S, Sickenberger W. Axis-free correction of astigmatism using bifocal soft contact lenses. Contact Lens and Anterior Eye. 2017;40(6):394-400. doi: https://doi.org/10.1016/j.clae.2017.09.002.

8.	Young G. Influence of Soft Contact Lens Design on Clinical Performance. Optometry and Vision Science. 1993;70(5):394-403.

9.	Strachan JPF. Some principles of the optics of hydrophilic lenses and geometrical optics applied to flexible lenses. The Australian Journal of Optometry. 1973;56(1):25-33. doi: 10.1111/j.1444-0938.1973.tb01065.x.

10.	Sarver MD, Harris MG, Polse KA. Corneal curvature and supplemental power effect of the Bausch and Lomb SOFLENS contact lens. Am J Optom Physiol Opt. 1975;52(7):470-3. Epub 1975/07/01. PubMed PMID: 1180322.

11.	Patel S. A theoretical model for predicting parameter changes in soft contact lenses due to bending. American journal of optometry and physiological optics. 1980;57(10):697-710. PubMed PMID: 7446678.

12.	Holden BA, Siddle J, Robson G, Zantos S. Soft Lens Performance Models: The Clinical Significance of the Lens Flexure Effect. The Australian Journal of Optometry. 1976;59:117-29.

13.	Weissman BA, Zisman F. Changes in back radius of soft contact lenses when flexed. Am J Optom Physiol Opt. 1979;56(10):613-7. Epub 1979/10/01. doi: 10.1097/00006324-197910000-00002. PubMed PMID: 525664.

14.	Janoff L, Dabezies OHJ. Power Change Induced by Soft Contact Lens Flexure. Eye & Contact Lens. 1983;9(1):32-8. PubMed PMID: 00003018-198301000-00008.

526 15. Weissman BA. A general relation between changing surface radii of flexing soft contact

527 lenses. Am J Optom Physiol Opt. 1984;61(10):651-3. Epub 1984/10/01. PubMed PMID: 6496642.

528 16. Holden BA, Zantos SG. On the conformity of soft lenses to the shape of the cornea. Am J

529 Optom Physiol Opt. 1981;58(2):139-43. Epub 1981/02/01. doi: 10.1097/00006324-198102000-

530 00004. PubMed PMID: 7223840.

531 17. Tomlinson A, Bibby MM. Movement and rotation of soft contact lenses. Effect of fit and lens

532 design. American journal of optometry and physiological optics. 1980;57(5):275-9. PubMed PMID:

533 7386591.

534 18. Momeni-Moghaddam H, Naroo SA, Askarizadeh F, Tahmasebi F. Comparison of fitting

535 stability of the different soft toric contact lenses. Cont Lens Anterior Eye. 2014;37(5):346-50. Epub

536 2014/06/05. doi: 10.1016/j.clae.2014.05.003. PubMed PMID: 24894546.

537 19. Whittle J. Contact lens optics and lens design. Eye. 2007;21:1022. doi:

538 10.1038/sj.eye.6702607.

539 20. Morgan PB, Woods CA, Tranoudis IG, Efron N, Jones L, Aighamdi W, et al. International

540 contact lens prescribing in 2018. Contact Lens Spectrum. 2019;34:26-32.

541 21. Young G, Allsopp G, Inglis A, Watson S. Comparative performance of disposable soft

542 contact lenses. Cont Lens Anterior Eye. 1997;20(1):13-21. Epub 1997/01/01. doi: 10.1016/s1367-

543 0484(97)80031-8. PubMed PMID: 16303343.

544 22. Efron N, Young G. Soft Lens Design and Fitting. Contact Lens Practice E-Book

545 Elsevier Health Sciences; 2016. p. 86-90.

546 23. de la Jara PL, Sankaridurg P, Ehrmann K, Holden BA. Influence of contact lens power profile

547 on peripheral refractive error. Optom Vis Sci. 2014;91(6):642-9. Epub 2014/05/09. doi:

548 10.1097/opx.0000000000000273. PubMed PMID: 24811847.

549 24. Grant R. Mechanics of toric soft lens stabilization. Journal of The British Contact Lens

550 Association. 1986;9:44-7. doi: https://doi.org/10.1016/S0141-7037(86)80023-4.

551 25. Fujikado T, Ninomiya S, Kobayashi T, Suzaki A, Nakada M, Nishida K. Effect of low-addition

552 soft contact lenses with decentered optical design on myopia progression in children: a pilot study.

553 Clinical ophthalmology (Auckland, NZ). 2014;8:1947-56. Epub 2014/10/07. doi:

554 10.2147/opth.S66884. PubMed PMID: 25284981; PubMed Central PMCID: PMCPMC4181743.

555 26. Young G, McIlraith R, Hunt C. Clinical evaluation of factors affecting soft toric lens

556 orientation. Optometry and Vision Science. 2009;86(11):E1259-E66.

557 27. Zhao G, Wollmer P. Surface activity of tear fluid. Acta Ophthalmol Scand. 1998;76:438–41.

558 28. Sulley A, Hawke R, Lorenz KO, Toubouti Y, Olivares G. Resultant vertical prism in toric soft

559 contact lenses. Contact Lens and Anterior Eye. 2015;38(4):253-7. doi:

560 https://doi.org/10.1016/j.clae.2015.02.006.

561 29.   Gilani F, Cortese M, Ambrosio Jr R, Lopes B, Ramos I, Harvey EM, et al. Comprehensive

562 anterior segment normal values generated by rotating Scheimpflug tomography. Journal of cataract

563 and refractive surgery. 2013;39:1707–12.

564 30.   Moore J, Lopes BT, Eliasy A, Geraghty B, Wu R, White L, et al. Simulation of the Effect of

565 Material Properties on Soft Contact Lens On-Eye Power. Bioengineering (Basel, Switzerland).

566 2019;6(4). Epub 2019/10/12. doi: 10.3390/bioengineering6040094. PubMed PMID: 31600967.

567 31.   Abass A, Lopes BT, Eliasy A, Salomao M, Wu R, White L, et al. Artefact-free topography

568 based scleral-asymmetry. PLOS ONE. 2019;14(7):e0219789. doi: 10.1371/journal.pone.0219789.

569 32.   Young G. 8 - Soft Lens Design and Fitting. Efron N, editor: Elsevier; 2018.

570 33.   Elsheikh A, McMonnies CW, Whitford C, Boneham GC. In vivo study of corneal responses to

571 increased intraocular pressure loading. Eye and vision (London, England). 2015;2:20-. doi:

572 10.1186/s40662-015-0029-z. PubMed PMID: 26693165.

573 34.   Elsheikh A. Finite element modeling of corneal biomechanical behavior. J Refract Surg.

574 2010;26(4):289-300. Epub 2010/04/27. doi: 10.3928/1081597x-20090710-01. PubMed PMID:

575 20415325.

576 35.   Abass A, Lopes BT, Eliasy A, Wu R, Jones S, Clamp J, et al. Three-dimensional non-

577 parametric method for limbus detection. PLOS ONE. 2018;13(11):e0207710. doi:

578 10.1371/journal.pone.0207710.

579 36.   Maurice DM. CHAPTER 6 - The Cornea and Sclera. In: Davson H, editor. Vegetative

580 Physiology and Biochemistry: Academic Press; 1962. p. 289-368.

581 37.   Jesus DA, Iskander R. Estimation of the Corneal Limbus with Zernike Polynomials using

582 Anterior Eye Topography. VII European World Meeting in Visual and Physiological Optics; August

583 2014; At Wroclaw, Poland2014.

584 38.   Al-Ageel S, Al-Muammar AM. Comparison of central corneal thickness measurements by

585 Pentacam, noncontact specular microscope, and ultrasound pachymetry in normal and post-LASIK

586 eyes. Saudi journal of ophthalmology : official journal of the Saudi Ophthalmological Society.

587 2009;23(3-4):181-7. Epub 2009/10/01. doi: 10.1016/j.sjopt.2009.10.002. PubMed PMID: 23960858;

588 PubMed Central PMCID: PMCPMC3729515.

589 39.   Fares U, Otri AM, Al-Aqaba MA, Dua HS. Correlation of central and peripheral corneal

590 thickness in healthy corneas. Cont Lens Anterior Eye. 2012;35(1):39-45. Epub 2011/09/03. doi:

591 10.1016/j.clae.2011.07.004. PubMed PMID: 21885326.

592 40.   Vurgese S, Panda-Jonas S, Jonas JB. Scleral thickness in human eyes. PLoS One.

593 2012;7(1):e29692. Epub 2012/01/13. doi: 10.1371/journal.pone.0029692. PubMed PMID:

594 22238635; PubMed Central PMCID: PMCPMC3253100.

595 41.   Elsheikh A, Geraghty B, Alhasso D, Knappett J, Campanelli M, Rama P. Regional variation

596 in the biomechanical properties of the human sclera. Experimental Eye Research. 2010;90:624-33.

597 doi: 10.1016/j.exer.2010.02.010. PubMed PMID: S0014483510000576.

598   42.   Elsheikh A, Whitford C, Hamarashid R, Kassem W, Joda A, Buchler P. Stress free

599   configuration of the human eye. Med Eng Phys. 2013;35(2):211-6. Epub 2012/10/09. doi:

600   10.1016/j.medengphy.2012.09.006. PubMed PMID: 23041490.

601   43.   Wang YX, Xu L, Wei WB, Jonas JB. Intraocular pressure and its normal range adjusted for

602   ocular and systemic parameters. The Beijing Eye Study 2011. PLoS One. 2018;13(5):e0196926.

603   Epub 2018/05/18. doi: 10.1371/journal.pone.0196926. PubMed PMID: 29771944; PubMed Central

604   PMCID: PMCPMC5957383 patent holder with Biocompatibles UK Ltd. (Franham, Surrey, UK) (Title:

605   Treatment of eye diseases using encapsulated cells encoding and secreting neuroprotective factor

606   and / or anti-angiogenic factor; Patent number: 20120263794), and has a patent application with

607   University of Heidelberg (Heidelberg, Germany) (Title: Agents for use in the therapeutic or

608   prophylactic treatment of myopia or hyperopia; Europaische Patentanmeldung 15 000 771.4). This

609   does not alter our adherence to PLOS ONE policies on sharing data and materials. All other authors

610   declare that no other competing interests exist.

611   44.   Shaw AJ, Collins MJ, Davis BA, Carney LG. Eyelid pressure and contact with the ocular

612   surface. Investigative ophthalmology & visual science. 2010;51(4):1911-7. doi: 10.1167/iovs.09-

613   4090. PubMed PMID: 19834035.

614   45.   Kwon K-A, Shipley RJ, Edirisinghe M, Ezra DG, Rose G, Best SM, et al. High-speed camera

615   characterization of voluntary eye blinking kinematics. Journal of The Royal Society Interface.

616   2013;10(85):20130227. doi: doi:10.1098/rsif.2013.0227.

617   46.   Sterner O, Aeschlimann R, Zürcher S, Osborn Lorenz K, Kakkassery J, Spencer ND, et al.

618   Friction Measurements on Contact Lenses in a Physiologically Relevant Environment: Effect of

619   Testing Conditions on Friction. Investigative ophthalmology & visual science. 2016;57(13):5383-92.

620   doi: 10.1167/iovs.16-19713.

621   47.   Khurana AK. Theory And Practice Of Optics And Refraction. 3 ed. India: Elsevier India Pvt.

622   Limited; 2008.

623   48.   Marsaglia G, Tsang WW, Wang J. Evaluating Kolmogorov's Distribution. Journal of

624   Statistical Software. 2003;008(i18).

625   49.   Everitt BS, Skrondal A. The Cambridge Dictionary of Statistics. 4 ed. Cambridge, UK:

626   Cambridge University Press; 2010.

627   50.   Kendall MG, Stuart A. The Advanced Theory of Statistics. Vol. 2: Inference and:

628   Relationsship: Griffin; 1973.

629   51.   Press WH, Teukolsky SA, Vetterling WT, Flannery BP. Numerical Recipes 3rd Edition: The

630   Art of Scientific Computing: Cambridge University Press; 2007.

631   52.   Bennett AG. Optics of Contact Lenses. 5 ed. London, UK: Association of Dispensing

632   Contacts; 1985. 99 p.

633   53.   Cavas-Martinez F, De la Cruz Sanchez E, Nieto Martinez J, Fernandez Canavate FJ,

634   Fernandez-Pacheco DG. Corneal topography in keratoconus: state of the art. Eye Vis (Lond).

635 2016;3:1-12. doi: 10.1186/s40662-016-0036-8. PubMed PMID: 26904709; PubMed Central PMCID:

636 PMCPMC4762162.

637 54.   Wolfe WL. Introduction to Imaging Spectrometers. USA: SPIE; 1997.

638 55.   Greivenkamp JE. Field Guide to Geometrical Optics. Washington USA: SPIE Press; 2004.

639 56.   Yang L, Huiyan Z. Shape preserving piecewise cubic interpolation. Applied Mathematics.

640 1996;11(4):419-24. doi: 10.1007/BF02662881.

641 57.   Geraghty B, Abass A, Eliasy A, Jones SW, Rama P, Kassem W, et al. Inflation experiments

642 and inverse finite element modelling of posterior human sclera. Journal of biomechanics.

643 2020;98:109438. Epub 2019/11/05. doi: 10.1016/j.jbiomech.2019.109438. PubMed PMID:

644 31679759.

645 58.   Ogden RW, Hill R. Large deformation isotropic elasticity - on the correlation of theory and

646 experiment for incompressible rubberlike solids. Proceedings of the Royal Society of London A

647 Mathematical and Physical Sciences. 1972;326(1567):565-84. doi: doi:10.1098/rspa.1972.0026.

648 59.   Elsheikh A, Wang D, Brown M, Rama P, Campanelli M, Pye D. Assessment of Corneal

649 Biomechanical Properties and Their Variation with Age. Current Eye Research. 2007;32(1):11-9.

650 doi: 10.1080/02713680601077145.

651 60.   Elsheikh A, Geraghty B, Rama P, Campanelli M, Meek KM. Characterization of age-related

652 variation in corneal biomechanical properties. Journal of the Royal Society Interface.

653 2010;7(51):1475-85. doi: 10.1098/rsif.2010.0108. PubMed PMID: 20392712; PubMed Central

654 PMCID: PMC2935603.

655

656

657

658

659

660

661

662

663

664

Appendix A: Axial and tangential radii of curvature

The least squares error method was applied to fit the best circle to each meridian and the radius of each fitted circle was used as a radius of curvature for this meridian. Local axial and tangential curvatures were calculated for 359 meridians with a 1.0° angular step covering the whole measured area of the cornea up to $x = 4$ mm radius.

While centres of axial curvatures were assumed to lie on the corneal visual axis (Fig 10), the centres of tangential curvature were free to be at any position but still within the relevant meridian plane (Fig 11). [53] As illustrated in Fig 10, the axial radius of curvature at any point is calculated as:

$$r = \frac{x}{\cos(90 - \alpha)} \qquad \text{Eq. 1}$$

where α is the tangent angle at this point. On the other hand, the tangential radius of curvature at any point, p_2, on the corneal surface can be calculated by fitting a circle to the three consecutive points $p_1(x_1, y_1, z_1)$, $p_2(x_2, y_2, z_2)$, $p_3(x_3, y_3, z_3)$ along the relevant meridian resulting in the value:

$$r = \frac{1}{2} \frac{\|p_1 - p_2\| \|p_2 - p_3\| \|p_3 - p_1\|}{(p_1 - p_2) \times (p_2 - p_3)} \qquad \text{Eq. 2}$$
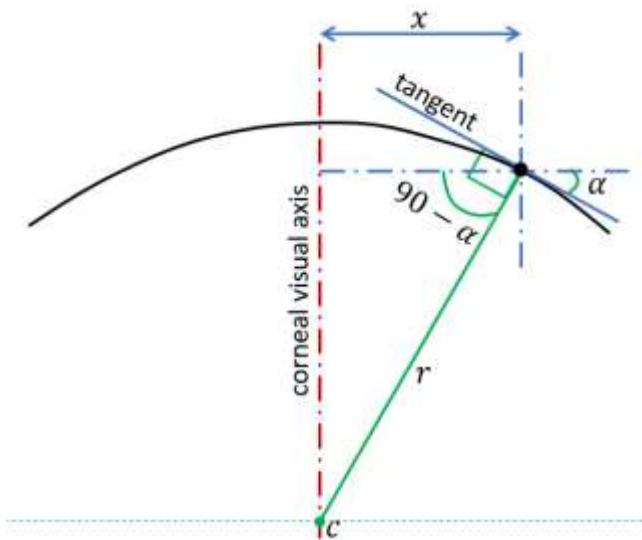
as illustrated in Fig 11.

Fig 10: Determination of corneal surface axial radius of curvature (r) at a certain meridian plane. In this method, the centre of the curvature (c) is always restricted to the corneal visual axis.
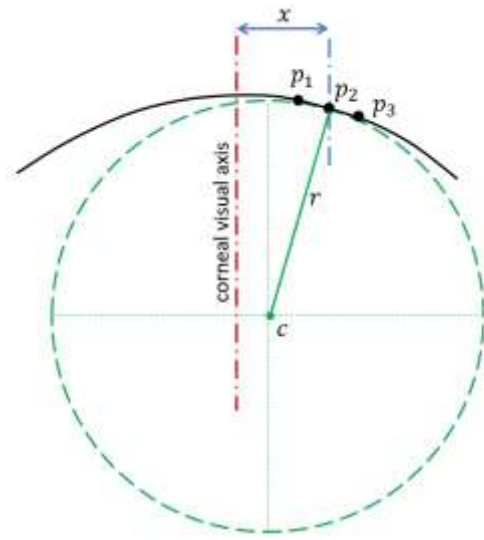
Fig 11: Determination of corneal surface tangential radius of curvature (r) at a certain meridian plane. In this method, the centre of the curvature (c) is not restricted to the corneal visual axis.

677

678   Both axial and tangential curvature map estimation methods handling local segments of each corneal

679   meridian as perfect circles, however, the method used for the axial curvature map calculation restricts

680   the surface curvature centres to the corneal visual axis.

681

682

683

684

685

686

687

688

689

Appendix B: Soft contact lens design

Back-surface design

Geometrical parameters considered in the design of the lens back-surface include the back optic zone radius or the base curve (R_{1b}), the back transient zone radius (R_{2b}), the peripheral curve radius (R_{3b}) and the overall lens diameter (d_3), Fig 3. As outlined in a previous study [5], X and Z coordinates (X_c, Z_c) of the centres of radii R_{1b}, R_{2b} and R_{3b} were calculated as:

$$X_{c1} = 0, \qquad Z_{c1} = -R_{1b} \qquad\qquad \text{Eq.1}$$

$$X_{c2} = 0, \qquad Z_{c2} = Z_{c1} - R_{2b} \cos\left(\sin^{-1}\frac{d_1}{2R_{2b}}\right) + R_{1b} \cos\left(\sin^{-1}\frac{d_1}{2R_{1b}}\right) \qquad \text{Eq.2}$$

$$X_{c3} = 0, \qquad Z_{c3} = Z_{c2} - R_{3b} \cos\left(\sin^{-1}\frac{d_2}{2R_{3b}}\right) + R_{2b} \cos\left(\sin^{-1}\frac{d_2}{2R_{2b}}\right) \qquad \text{Eq.3}$$

and the back-surface elevation, Z_b was constructed as

$$Z_b = \begin{cases} Z_{c1} + \sqrt{R_{1b}^2 - (X - X_{c1})^2} \quad, & 0 \le X < \dfrac{d_1}{2} - x_{p1} \\[2mm] Z_{c2} + \sqrt{R_{2b}^2 - (X - X_{c2})^2} \quad, & \dfrac{d_1}{2} + x_{p2} \le X < \dfrac{d_2}{2} - x_{p3} \\[2mm] Z_{c3} + \sqrt{R_{3b}^2 - (X - X_{c3})^2} \quad, & \dfrac{d_2}{2} + x_{p4} \le X \le \dfrac{d_3}{2} \end{cases} \qquad \text{Eq.4}$$

Front-surface design

A typical initial central lens thickness $T_c = 0.11$ mm was used in all cases before being updated during the design process (Fig 3). The lens material refractive index (n) was set to 1.334 to simulate hydrogel optical characteristics [5], however, the lens nominal power (P_i) was varied according to the required optical power to be consistent with the Lens Makers Equation (Eq. 5) which was solved for optic zone front-surface curve R_{1f} in Eq. 6

$$P_i = (n - 1)\left(\frac{1}{R_{1f}} - \frac{1}{R_{1b}} + \frac{T_c\,(n - 1)}{n\,R_{1f}\,R_{1b}}\right) \qquad\qquad \text{Eq. 5, [54, 55]}$$

$$R_{1fi} = \frac{T_c(n-1)^2 + n(n-1)R_{1b}}{nR_{1b}P_i + n(n-1)} \qquad\qquad \text{Eq. 6, [5, 30]}$$

704   Front-surfaces were designed with the lens shape factor (k) set to the empirically estimated value of

705   0.75 to eliminate the spherical aberration on the central vision zone, Therefore, the lens front-surface

706   was shaped meridian by meridian as:

$$Z_{fi} = T_c - \frac{1}{k}\left(R_{1fi} - \sqrt{R_{1fi}^2 - kX^2}\right) \qquad\qquad \text{Eq.7}$$

707   Where the subscript (i) stands for the meridian number and therefore i equals 1, 2, 3, …, 360

708   corresponding respectively to meridian angles θ = 0°, 1°, 359° rotating around the Z-axis in the anti-

709   clockwise direction.

710   **Fillet design**

711   To avoid sharp edges on the back-surface, fillets with radii r_1=2 mm and r_2=1.5 mm were introduced

712   to connect the sections of the back surface with curvature changes of R_{1b} to R_{2b}, and R_{2b} to R_{3b}

713   respectively, Fig 3. The centre of the r_1 fillet $(X_{c_{r1}}, Z_{c_{r1}})$ was calculated by finding the point at which

714   the two sections under consideration would intersect if their radii were reduced by the fillet radius, r_1.

715   When this problem was solved exactly, the following relations were achieved,

$$X_{c_{r1}} = \frac{Q_1\sqrt{Q_2 Q_3} - Z_{c2}\sqrt{Q_3 Q_4} - Q_5}{2Q_6} \quad , \quad Z_{c_{r1}} = Z_{c1} + \sqrt{(R_{1b}+r_1)^2 - (X_{cr1}-X_{c1})^2} \quad \text{Eq.8}$$

716   where X_{ci} and Z_{ci} denote the coordinates of the centre of radius R_{ib} and the variables denoted by Q

717   are shape factors, detailed in Table 2. The start and end points of the fillet were then computed by

718   finding the two locations where a circle with centre (X_{c1}, Z_{c1}) and radius r_1, intersects the lens surface.

719   The result of this is a start (x_{p1}, z_{p1}) and end point (x_{p2}, z_{p2}) for the fillet given by,

$$x_{p1} = \frac{Q_7 Q_8 - z_{cr1}Q_8 - 2Q_{10}}{2Q_{11}} \quad , \quad z_{p1} = Z_{c1} + \sqrt{R_{1b}^2 - (x_{p1}-X_{c1})^2} \qquad \text{Eq.9}$$

$$x_{p2} = \frac{Q_{12} Q_{13} - Z_{cr1}Q_{13} - 2Q_{15}}{2Q_{16}} \quad , \quad z_{p2} = Z_{c2} + \sqrt{R_{2b}^2 - (x_{p2}-X_{c2})^2} \qquad \text{Eq.10}$$

720

721 Applying the same process to the second change in lens geometry (R_{2b} to R_{3b}) yielded a fillet with

722 centroid $(X_{c_{r2}}, Z_{c_{r2}})$ and start (x_{p3}, z_{p3}) and end points (x_{p4}, z_{p4}) given by,

723

$$X_{cr2} = \frac{Q_{17}\sqrt{Q_{18}Q_{19}} + Z_{c3}\sqrt{Q_{18}Q_{19}} - 2Q_{20}}{2Q_{21}} \quad , \quad Z_{cr2} = Z_{c2} + \sqrt{(R_{2b} - r_2)^2 - (X_{cr2} - X_{c2})^2} \quad \text{Eq.11}$$

$$x_{p3} = \frac{Q_{22}\sqrt{|Q_{23}Q_{24}|} - Z_{cr2}\sqrt{|Q_{23}Q_{24}|} - 2Q_{25}}{2Q_{26}} \quad , \quad z_{p3} = Z_{c2} + \sqrt{R_{2b}^2 - (x_{p3} - X_{c2})^2} \quad \text{Eq.12}$$

$$x_{p4} = \frac{Q_{27}\sqrt{|Q_{28}Q_{29}|} - Z_{cr2}\sqrt{|Q_{28}Q_{29}|} - 2Q_{30}}{2Q_{31}} \quad , \quad z_{p4} = Z_{c3} + \sqrt{R_{3b}^2 - (x_{p4} - X_{c3})^2} \quad \text{Eq.13}$$

724

725 The new back surface coordinates for the regions occupied by fillets are then defined as,

$$Z_b = \begin{cases} Z_{cr1} - \sqrt{r_1^2 - (x - X_{cr1})^2} & , \quad x_{p1} \le x < x_{p2} \\ Z_{cr2} + \sqrt{r_2^2 - (x - X_{cr2})^2} & , \quad x_{p3} \le x \le x_{p4} \end{cases} \quad \text{Eq.14}$$

726 In all designs, the choice of base curve R_{1b}, transient zone R_{2b} and peripheral zone radii R_{3b} was

727 constrained such that,

$$R_{1b} = R_{2b} - 0.5 = R_{3b} - 1 \quad \text{(all dimensions in mm)} \quad \text{Eq.15}$$

728 The range of values used in the lens geometry design was chosen to cover the average dimensions

729 of the commercially available contact lenses. Base curve radius (back optic zone radius), R_{1b}, was set

730 to 8.20 mm, optic zone diameter d_1 was set to 8.00 mm, and finally, the lens overall lens diameter, d_3,

731 was set to 14.50 mm and d_2 to the mean value of d_1 and d_3.

732 Following the design of a two-dimensional lens profile, A three-dimensional back-surface profile was

733 constructed in 1° steps, meridian by meridian. This final step was necessary for the use of lens

734 geometry in both the finite element and light raytracing analysis.

735

736

Peripheral-zone design

737

738   Unlike the back-surface, the front-surface was not rotationally symmetric. The asymmetric nature of

739   the front surface meant that, when constructing the three-dimensional geometry, each meridian had

740   to be considered individually. The thickness of the boundary between the transient zone and the

741   periphery zone T_w was calculated in a way to allow the addition of thickness to certain meridians

742   according to the type of balance zone.

$$T_{w_i} = \begin{cases} 0.4W_i(2T + Tc)/3 & \text{for G1P design} \\ 0.3W_i(2T + Tc)/3 & \text{for B2P design} \\ 0.2W_i(2T + Tc)/3 & \text{for B4P design} \end{cases} \qquad \text{Eq.16}$$

743   where T is the lens thickness at the end of the optical zone ($X = \frac{d_1}{2}$), T_c is the central thickness of the

744   lens and W is a weighting factor defined as:

$$W = \begin{cases} \cos\left(\theta + \dfrac{\pi}{2}\right) & \text{for G1P design} \\ \cos(2\theta) & \text{for B2P design} \\ cos\,(4\theta + \pi) & \text{for B4P design} \end{cases} \qquad \text{Eq.17}$$

745   The weighting factor W was set to zero for meridian angles, θ, at which the calculated value was

746   negative.

747   Finally, the lens edge thickness (T_e) was set as a function of the optical power as $0.1+0.002|P_{max}|$

748   before fitting the lens's front-surface points via shape-preserving piecewise cubic interpolation [56] to

749   ensure a smooth front-surface while keeping the designed points in their position. In this design

750   configuration, P_{max} is either the summation of the spherical and cylindrical power or the spherical

751   power only, whichever was higher.

752   The lens central thickness (T_c) was then updated through an automatic loop to avoid producing

753   regions of negative volume resulting from the intersection of the front- and back-surfaces during the

754   lens design process. For each thickness change, R_{1f} and T_w were recalculated and the front-surface

755   Z_f was updated accordingly.

756

757   Table 2: Lens back-surface shape parameters

$Q_1 = R_{1b}^2 X_{c2} - R_{1b}^2 X_{c1} + R_{2b}^2 X_{c1} - R_{2b}^2 X_{c2} - X_{c1}X_{c2}^2 - X_{c1}^2 X_{c2} + X_{c1}Z_{c1}^2 + X_{c1}Z_{c2}^2 + X_{c2}Z_{c2}^2 + X_{c1}^3 + X_{c2}^3 + Z_{c1}$

$Q_2 = R_{1b}^2 + 2R_{1b}R_{2b} - R_{2b}^2 + X_{c1}^2 - 2X_{c1}X_{c2} + X_{c2}^2 + Z_{c1}^2 - 2Z_{c1}Z_{c2} + Z_{c2}^2$

$Q_3 = R_{1b}^2 + 2R_{1b}R_{2b} + 4R_{1b}r_1 + R_{2b}^2 + 4R_{2b}r_1 - X_{c1}^2 + 2X_{c1}X_{c2} - X_{c2}^2 - Z_{c1}^2 + 2Z_{c1}Z_{c2} - Z_{c2}^2 + 4r_1^2$

$Q_4 = -R_{1b}^2 + 2R_{1b}R_{2b} - R_{2b}^2 + X_{c1}^2 - 2X_{x1}X_{c2} + X_{c2}^2 + Z_{c1}^2 - 2Z_{c1}Z_{c2} + Z_{c2}^2$

$Q_5 = 2X_{c1}Z_{c1}Z_{c2} - 2X_{c2}Z_{c1}Z_{c2} - 2R_{1b}X_{c1}r_1 + 2R_{1b}X_{c2}r_1 + 2R_{2b}X_{c1}r_1 - 2R_{2b}X_{c2}r_1$

$Q_6 = X_{c1}^2 - 2X_{c1}X_{c2} + X_{c2}^2 + Z_{c1}^2 - 2Z_{c1}Z_{c2} + Z_{c2}^2$

$Q_7 = R_{1b}^2 X_{cr1} - R_{1b}^2 X_{c1} - X_{c1}X_{cr1}^2 - X_{c1}^2 X_{cr1} + X_{c1}Z_{c1}^2 + X_{c1}Z_{cr1}^2 + X_{cr1}Z_{c1}^2 + X_{cr1}Z_{cr1}^2 + X_{c1}r_1^2 - X_{cr1}r_1^2 + X_{c1}^3 + X_{cr1}^3 + Z_{c1}$

$Q_8 = R_{1b}^2 + 2R_{1b}r_1 - X_{c1}^2 + 2X_{c1}X_{cr1} - X_{cr1}^2 - Z_{c1}^2 + 2Z_{c1}Z_{cr1} - Z_{cr1}^2 + r_1^2$

$Q_9 = -R_{1b}^2 + 2R_{1b}r_1 + X_{c1}^2 - 2X_{c1}X_{cr1} + X_{cr1}^2 + Z_{c1}^2 - 2Z_{c1}Z_{cr1} + Z_{cr1}^2 - r_1^2$

$Q_{10} = X_{c1}Z_{c1}Z_{cr1} + X_{cr1}Z_{c1}Z_{cr1}$

$Q_{11} = X_{c1}^2 - 2X_{c1}X_{cr1} + X_{cr1}^2 + Z_{c1}^2 - 2Z_{c1}Z_{cr1} + Z_{cr1}^2$

$Q_{12} = R_{2b}^2 X_{cr1} - R_{2b}^2 X_{c2} - X_{c2}X_{cr1}^2 - X_{c2}^2 X_{cr1} + X_{c2}Z_{c2}^2 + X_{c2}Z_{cr1}^2 + X_{cr1}Z_{c2}^2 + X_{cr1}Z_{cr1}^2 + X_{c2}r_1^2 - X_{cr1}r_1^2 + X_{c2}^3 + X_{cr1}^3 + Z_{c2}$

$Q_{13} = R_{2b}^2 + 2R_{2b}r_1 - X_{c2}^2 + 2X_{c2}X_{cr1} - X_{cr1}^2 - Z_{c2}^2 + 2Z_{c2}Z_{cr1} - Z_{cr1}^2 + r_1^2$

$Q_{14} = -R_{2b}^2 + 2R_{2b}r_1 + X_{c2}^2 - 2X_{c2}X_{cr1} + X_{cr1}^2 + Z_{c2}^2 - 2Z_{c2}Z_{cr1} + Z_{cr1}^2 - r_1^2$

$Q_{15} = X_{c2}Z_{c2}Z_{cr1} + X_{cr1}Z_{c2}Z_{cr1}$

$Q_{16} = X_{c2}^2 - 2X_{c2}X_{cr1} + X_{cr1}^2 + Z_{c2}^2 - 2Z_{c2}Z_{cr1} + Z_{cr1}^2$

$Q_{17} = R_{2b}^2 X_{c3} - R_{2b}^2 X_{c2} + R_{3b}^2 X_{c2} - R_{3b}^2 X_{c3} - X_{c2}X_{c3}^2 - X_{c2}^2 X_{c3} + X_{c2}Z_{c2}^2 + X_{c2}Z_{c3}^2 + X_{c3}Z_{c2}^2 + X_{c2}^3 + X_{c3}^3 - Z_{c2}$

$Q_{18} = -R_{2b}^2 + 2R_{2b}R_{3b} - R_{3b}^2 + X_{c2}^2 - 2X_{c2}X_{c3} + X_{c3}^2 + Z_{c2}^2 - 2Z_{c2}Z_{c3} + Z_{c3}^2$

$Q_{19} = R_{2b}^2 + 2R_{2b}R_{3b} - 4R_{2b}r_2 + R_{3b}^2 - 4R_{3b}r_2 - X_{c2}^2 + 2X_{c2}X_{c3} - X_{c3}^2 - Z_{c2}^2 + 2Z_{c2}Z_{c3} - Z_{c3}^2 + 4r_2^2$

$Q_{20} = X_{c2}Z_{c2}Z_{c3} + X_{c3}Z_{c2}Z_{c3} - R_{2b}X_{c2}r_2 + R_{2b}X_{c3}r_2 + R_{3b}X_{c2}r_2 - R_{3b}X_{c3}r_2$

$Q_{21} = X_{c2}^2 - 2X_{c2}X_{c3} + X_{c3}^2 + Z_{c2}^2 - 2Z_{c2}Z_{c3} + Z_{c3}^2$

$Q_{22} = R_{2b}^2 X_{cr2} - R_{2b}^2 X_{c2} - X_{c2}X_{cr2}^2 - X_{c2}^2 X_{cr2} + X_{c2}Z_{c2}^2 + X_{c2}Z_{cr2}^2 + X_{cr2}Z_{c2}^2 + X_{cr2}Z_{cr2}^2 + X_{c2}r_2^2 - X_{cr2}r_2^2 + X_{c2}^3 + X_{cr2}^3 + Z_{c2}$

$Q_{23} = R_{2b}^2 + 2R_{2b}r_2 - X_{c2}^2 + 2X_{c2}X_{cr2} - X_{cr2}^2 - Z_{c2}^2 + 2Z_{c2}Z_{cr2} - Z_{cr2}^2 + r_2^2$

$Q_{24} = -R_{2b}^2 + 2R_{2b}r_2 + X_{c2}^2 - 2X_{c2}X_{cr2} + X_{cr2}^2 + Z_{c2}^2 - 2Z_{c2}Z_{cr2} + Z_{cr2}^2 - r_2^2$

$Q_{25} = X_{c2}Z_{c2}Z_{cr2} + X_{cr2}Z_{c2}Z_{cr2}$

$Q_{26} = X_{c2}^2 - 2X_{c2}X_{cr2} + X_{cr2}^2 + Z_{c2}^2 - 2Z_{c2}Z_{cr2} + Z_{cr2}^2$

$Q_{27} = R_{3b}^2 X_{cr2} - R_{3b}^2 X_{c3} - X_{c3}X_{cr2}^2 - X_{c3}^2 X_{cr2} + X_{c3}Z_{c3}^2 + X_{c3}Z_{cr2}^2 + X_{cr2}Z_{c3}^2 + X_{cr2}Z_{cr2}^2 + X_{c3}r_2^2 - X_{cr2}r_2^2 + X_{c3}^3 + X_{cr2}^3 + Z_{c3}$

$Q_{28} = R_{3b}^2 + 2R_{3b}r_2 - X_{c3}^2 + 2X_{c3}X_{cr2} - X_{cr2}^2 - Z_{c3}^2 + 2Z_{c3}Z_{cr2} - Z_{cr2}^2 + r_2^2$

$Q_{29} = -R_{3b}^2 + 2R_{3b}r_2 + X_{c3}^2 - 2X_{c3}X_{cr2} + X_{cr2}^2 + Z_{c3}^2 - 2Z_{c3}Z_{cr2} + Z_{cr2}^2 - r_2^2$

$Q_{30} = X_{c3}Z_{c3}Z_{cr2} + X_{cr2}Z_{c3}Z_{cr2}$

$Q_{31} = X_{c3}^2 - 2X_{c3}X_{cr2} + X_{cr2}^2 + Z_{c3}^2 - 2Z_{c3}Z_{cr2} + Z_{cr2}^2$
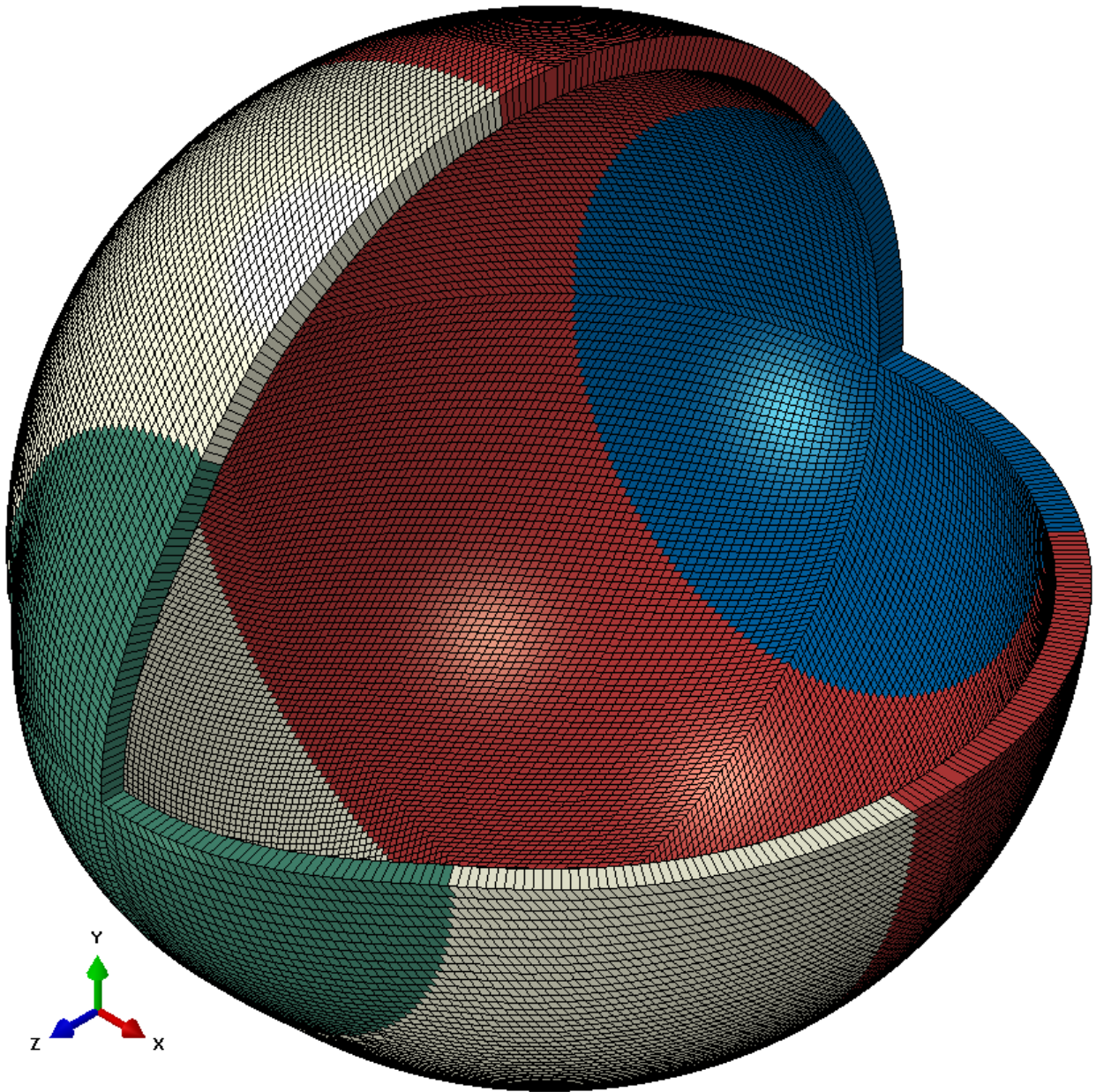
758

759

Appendix C: Material models

The eye was modelled as hyper-elastic soft tissue with a water-like density of 1000 kg/m^3 and four regions including the cornea (μ_c=0.07, α_c=110.8), anterior, intermediate and posterior sclera separated at elevation angles of 55°, 7.5°, -47.5° measured from the centre of the sclera [57], Fig 12. First-order Ogden material models [58] were used to represent the eye tissue's mechanical performance with different stress-strain behaviour under loading conditions following earlier experimental studies [57, 59, 60], Fig 13. The purpose of splitting the sclera into three regions was to characterise regional mechanical properties of scleral tissue using circumferential regions of isotropic elements to replicate macroscale sclera displacements. Scleral materials were characterised as μ_{s1}=0.441, α_{s1}=124.5, μ_{s2}=0.349, α_{s2}=138.5, μ_{s3}=0.308 and α_{s3}=162.2.
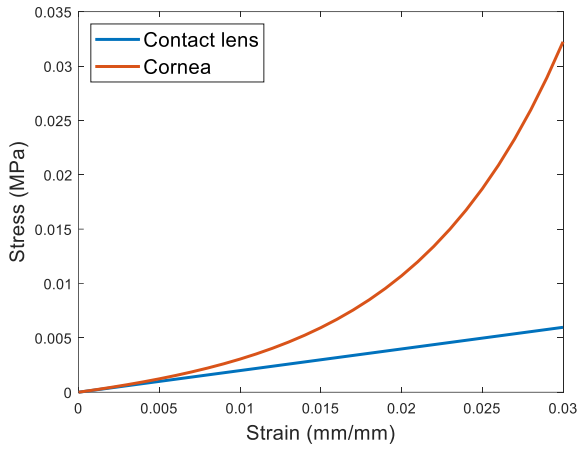
Each contact lens from the three investigated soft contact lens designs (G1P, B2P & B4P) was modelled as an incompressible linear elastic solid with a Young's modulus of 0.199 MPa, a Poisson's ratio of 0.49 and the density of water 1000 kg/m^3 [30].
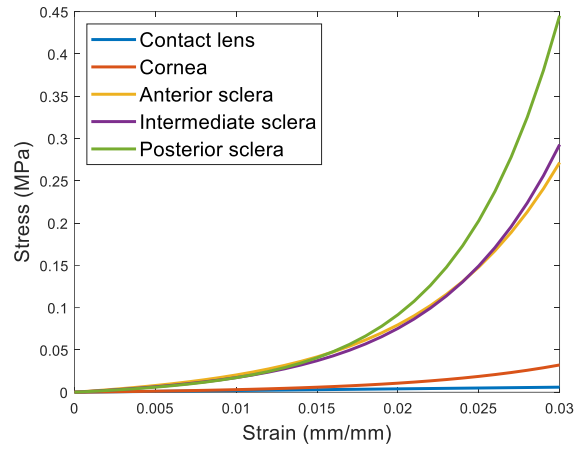
773

Fig 12: A typical FE model for the average eye used in this study where different colours represent

different material models. The eye's equatorial nodes were constrained in axial directions.

776

(a)   (b)

Fig 13: Stress-strain curves for the material models. Contact lens's material was modelled as a linear elastic material, however, the eye was modelled as a hyper-elastic material.